UCLA
UCLA Previously Published Works

Title

Turning on Low-Temperature Catalytic Conversion of Biomass Derivatives through Teaming Pd1 and Mo1 Single-Atom Sites

Permalink

https://escholarship.org/uc/item/9mc5k1wk

Journal

Journal of the American Chemical Society, 146(47)

ISSN

0002-7863

Authors

Tang, Yu

Yan, George

Zhang, Shiran

et al.

Publication Date

2024-11-27

DOI

10.1021/jacs.4c07075

Supplemental Material

https://escholarship.org/uc/item/9mc5k1wk#supplemental

Copyright Information

Peer reviewed

Turning on Low-Temperature Catalytic Conversion of Biomass Derivatives through Teaming Pd₁ and Mo₁ Single-Atom Sites

Yu Tang,[a,¶] George Yan,[b,¶] Shiran Zhang,[a,¶] Yuting Li,[a,¶] Luan Nguyen,[a] Yasuhiro Iwasawa,[c] Tomohiro Sakata,[c] Christopher Andolina,[d] Judith C. Yang,[d] Philippe Sautet,[b,e*] Franklin Feng Tao[a*]

[a] Center for Environmental Beneficial Catalysis and Department of Chemical and Petroleum Engineering, University of Kansas, Lawrence, KS 66045, USA.
[b] Department of Chemical and Biomolecular Engineering, University of California, Los Angeles, CA 90095, USA.
[c] Innovation Research Center for Fuel Cells and Graduate School of Informatics and Engineering, The University of Electro-Communications, Chofu, Tokyo 182-8585, Japan.
[d] Department of Chemical and Petroleum Engineering, University of Pittsburgh, Pittsburgh, PA, 15261, USA
[e] Department of Chemistry and Biochemistry, University of California, Los Angeles, CA 90095, USA.

¶: These authors made equal contribution to this work.

*: To whom all correspondence should be addressed to. Email: franklin.tao.2017@gmail.com (FT) and sautet@ucla.edu (PS)

Abstract

On purpose atomic scale design of catalytic sites specifically active and selective at low temperature for a target reaction is a key challenge. Here we report teamed Pd_1 and Mo_1 single-atom sites that exhibit high activity and selectivity for anisole hydrodeoxygenation to benzene at low temperature, 100-150°C where a Pd metal nanoparticle catalyst or a MoO_3 nanoparticle catalyst is individually inactive. The catalyst built from Pd_1 or Mo_1 single-atom sites alone are much less effective, although the catalyst with Pd_1 sites shows some activity but low selectivity. Similarly, less dispersed nanoparticle catalysts are much less effective. Computational studies show that the Pd_1 and Mo_1 single-atom sites activate H_2 and anisole, respectively and their combination triggers the hydrodeoxygenation of anisole in this low temperature range. The Co_3O_4 support is inactive for anisole hydrodeoxygenation by itself but participates in the chemistry by transferring H atoms from the Pd_1 to the Mo_1 site. This finding opens an avenue of designing catalysts active for a target reaction channel such as conversion of biomass derivatives at a low temperature where neither metal nor oxide nanoparticles are.

Keywords: Single-atom catalysis, multifunctional catalysis, hydrodeoxygenation, catalysis, in situ spectroscopy, density functional theory calculations, and kinetic modeling

1. Introduction

The on-purpose design at the atomic scale of catalysts for multi-step reactions that would operate at low temperature with high selectivity is the "holy grail" of heterogeneous catalysis. Usual heterogeneous catalysts, formed by nanoparticles of metal or oxide on a support present a variety of active sites. In many situations, this wide, but nonuniform, distribution of active sites on metal or oxide nanoparticles may suppress activity and selectivity at low temperature due to potential poisoning of some types of active sites to decrease the per-atom activity of the catalyst and unwanted side-reactions.[1-4] Highly dispersed catalytic sites, ultimately in the form of isolated cations, present a narrow distribution of uniform active sites with specific electronic structures, which may improve the catalytic activity and selectivity. The downside of this specificity is that such single atoms may have difficulty in catalyzing a multi-step reaction.[5, 6]

Here, to realize catalysis along a demanded reaction channel at a low temperature where supported metal or oxide nanoparticle catalysts of metal element X or Y are not active, we propose teaming two single-atom sites including X_1, responsible for chemisorbing and activating molecule A, and Y_1 for molecule B, respectively, to turn on the reaction between A and B at low temperature. Here the subscript "1" was added to refer to a single-atom site. Typically, single-atom sites are formed by immobilization of an isolated metal cation on an oxide support and have a chemical state and coordination environment markedly different from that of the continuously packed surface sites of a nanoparticle of the considered metal.[7, 8]

To explore the hypothesis of realizing low-temperature catalysis through teaming single-atom sites, hydrodeoxygenation (HDO), a transformative reaction of biomass derivative,[9-13] was chosen as a probe reaction. Single-atom Pd_1 and Mo_1 sites were chosen to anchor on Co_3O_4. Our exploration shows that Pd_1 and Mo_1 single-atom sites activate H_2 and anisole, respectively, and

that the teamed Pd_1 and Mo_1 single-atom catalyst is highly active and selective for anisole HDO at a temperature as low as 100^oC, while neither a Pd metal nanoparticle nor a MoO_3 nanoparticle is active for producing benzene through anisole HDO in the temperature range 25^oC-250^oC.[13] This work demonstrates that teaming single-atom catalytic sites is an efficient approach for designing catalysts active and selective at low temperature.

2. Results and Discussion

2.1 Preparation and in-situ characterization of catalyst with teamed Pd_1 and Mo_1 single-atom sites

2.1.1 Selection of reaction and design of catalysts

We chose the hydrodeoxygenation (HDO) of anisole [11, 14-25] as an example of a type of reactions in which both reactants, molecular hydrogen and anisole, must be adsorbed and dissociated on catalytic sites before their derivatives could couple to form intermediates leading to a product such as benzene. Palladium metal nanoparticles supported on silica, 0.5wt%Pd/SiO_2 [**Figures S9 and S10 in the Supporting Information (SI)**] were first prepared as benchmark materials through impregnation of a palladium precursor, followed by drying at 60^oC in air and then reduction at 350^oC in H_2. These supported Pd nanoparticles are not active for anisole HDO at <300^oC although they are active for hydrogenation of anisole to methoxycyclohexane (**Figure S19**). MoO_3 nanoparticles are not active for anisole HDO at a temperature lower than 250^oC (**Figure S20**), consistent with literature.[13] In addition, literature reported that MoO_3 crystallites undergo facile reduction to form less reactive MoO_2 at 320^oC.[26]
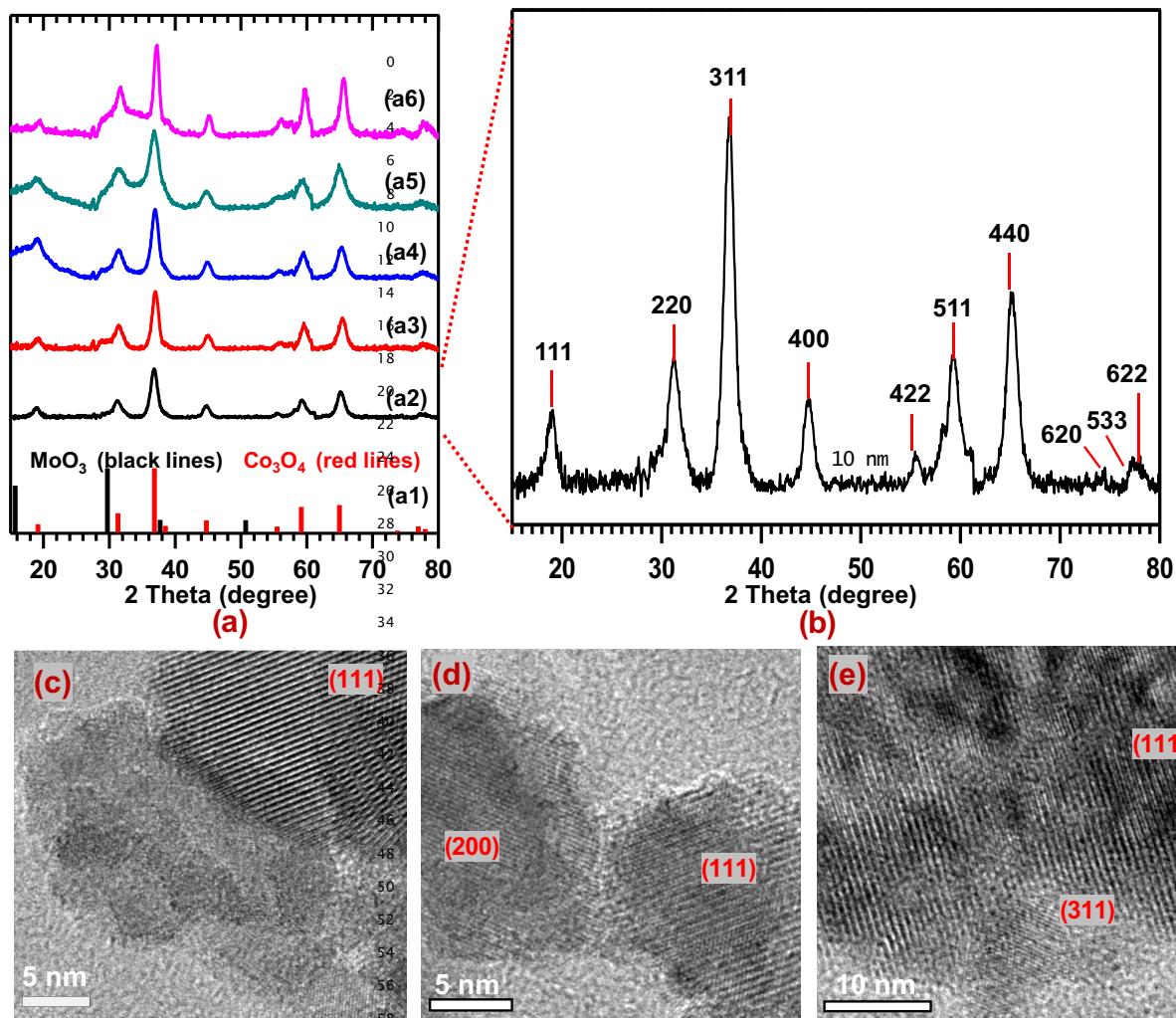
Figure 1. XRD and TEM studies of used catalysts. (a) XRD patterns of MoO_3 (black line) and Co_3O_4 (red line) (a1), used $0.25wt\%Pd/(Co_{0.95}Mo_{0.05})_3O_4$ (a2), $0.25wt\%Pd/Co_3O_4$ (a3), $5.0\%Mo/Co_3O_4$ (a4), $0.25wt\%Pd/(Co_{0.90}Mo_{0.10})_3O_4$ (a5), and $0.25wt\%Pd/(Co_{0.80}Mo_{0.20})_3O_4$ (a6). (b) Enlargement of XRD pattern of $0.25wt\%Pd/(Co_{0.95}Mo_{0.05})_3O_4$ after anisole HDO at 150°C. (c-e) High-resolution TEM images of $0.25wt\%Pd/(Co_{0.95}Mo_{0.05})_3O_4$ nanoparticles after anisole HDO at 150°C.

To prove the hypothesis that teaming single-atom sites could turn on anisole HDO catalysis at low temperature, we chose palladium as one of the two metal elements as it was demonstrated in the literature that (1) singly dispersed Pd atoms (Pd_1) on Cu or Au metal can activate molecular hydrogen at low temperature and (2) the adsorption energy of H atoms on Pd_1 single-atom sites is relatively weak and thus allows H atoms to spill-over on the support.[27-30] In addition, we chose isolated Mo_1 cations as the second type of single-atom sites since they exhibit

5

high affinity to oxygen atoms.[31-34] We selected Co_3O_4 as the support to anchor Pd_1 and Mo_1 atoms as it has been used as a support for Pt,[35] Pd,[36] Ni[37], and Rh[38, 39] single-atoms in the literature.

2.1.2 Preparation of catalysts

Three catalysts, $(Co_{0.95}Mo_{0.05})_3O_4$ having only single-atom Mo_1 sites (Mo_1/Co_3O_4), $0.25wt\%Pd/Co_3O_4$ having only single-atom Pd_1 sites (Pd_1/Co_3O_4), and $0.25wt\%Pd/(Co_{0.95}Mo_{0.05})_3O_4$ having coexisting single-atom Mo_1 sites and single-atom Pd_1 ones (Pd_1+Mo_1/Co_3O_4), respectively, were prepared (**Section S1 of the SI**). To prepare $0.25wt\%Pd/(Co_{0.95}Mo_{0.05})_3O_4$, $(Co_{0.95}Mo_{0.05})_3O_4$ was first prepared by a wet-chemistry route and then Pd was added in a second step by a specific deposition-precipitation as described in SI. XRD patterns of the used $(Co_{0.95}Mo_{0.05})_3O_4$, $0.25wt\%Pd/Co_3O_4$, and $0.25wt\%Pd/(Co_{0.95}Mo_{0.05})_3O_4$ are presented in **Figure 1a2, 1a3, and 1a4**, respectively. Since the three used catalysts exhibit the same XRD pattern as pure Co_3O_4 (the red lines in **Figure 1a1**), the introduction of Pd_1 and/or Mo_1 atoms in the three catalysts did not change the lattice structure of the Co_3O_4 support. Sizes of $0.25wt\%Pd/(Co_{0.95}Mo_{0.05})_3O_4$ nanoparticles are 10 ± 2 nm before catalysis and 11 ± 3 nm after catalysis, based on calculations using the Scherrer equation[40] based on its XRD pattern in Figures 1b and statistical accounting of TEM images such as **Figure 1c-1e** and **Figure S2**. These studies suggest that no notable sintering of $0.25wt\%Pd/(Co_{0.95}Mo_{0.05})_3O_4$ nanoparticles occurred after the anisole HDO at 150°C. In addition, the crystalline nature of the support of $0.25wt\%Pd/(Co_{0.95}Mo_{0.05})_3O_4$ after HDO catalysis at 150°C was confirmed by the observation of lattice fringes of the (111), (200) and (311) planes of Co_3O_4 in HRTEM images

(**Figure 1c-1e**). Statistical investigations suggest that the main exposed plane of the Co_3O_4 nanoparticles is (111).

2.1.3 XANES and EXAFS studies of fresh $0.25wt\%Pd/(Co_{0.95}Mo_{0.05})_3O_4$

The oxidations state and coordination environment of Pd and Mo atoms of the fresh catalyst $0.25wt\%Pd/(Co_{0.95}Mo_{0.05})_3O_4$ were characterized with X-ray Absorption Near Edge Spectroscopy (XANES)[41], Extended X-ray Absorption Fine Structure (EXAFS)[42], and Ambient Pressure X-ray Photoelectron Spectroscopy (AP-XPS)[43, 44] in a manner of ex situ studies at 25^oC and in situ studies at catalysis temperatures under a catalytic condition as defined by the literature.[45] The Pd foil, Mo foil, and PdO nanoparticles in ambient were studied as references for energy calibration and peak assignment in XAS studies. Their XANES spectra of Pd K-edge and Mo K-edge and their r-space spectra of Pd foil, Mo foil, and PdO nanoparticles were generated to aid the interpretation of energy-space and r-space spectra of $0.25wt\%Pd/(Co_{0.95}Mo_{0.05})_3O_4$ before catalysis, also designated as fresh catalyst, and $0.25wt\%Pd/(Co_{0.95}Mo_{0.05})_3O_4$ during catalysis, anisole HDO at 150^oC.

The red spectrum in **Figure 2b** is the energy space spectrum of Mo K-edge of the fresh catalyst, $0.25wt\%Pd/(Co_{0.95}Mo_{0.05})_3O_4$. It is distinctly different from the black spectrum of Mo foil in **Figure 2b** but similar to MoO_3 reported in literature.[46] Thus, Mo atoms of the fresh catalyst $0.25wt\%Pd/(Co_{0.95}Mo_{0.05})_3O_4$ are oxidized. In addition, the r-space spectrum of Mo K-edge of the fresh catalyst (black spectrum in **Figure 2d**) is distinctly different from the Mo foil (pink spectrum in **Figure 2d**). The fresh $0.25wt\%Pd/(Co_{0.95}Mo_{0.05})_3O_4$ has one major peak at 1.71 Å while there is a minor peak at 3.23 Å (black spectrum in **Figure 2d**). All distances cited in this article are the values upon phase correction of EXAFS unless a specific note is given.

Based on the literature[46], the Mo-O-Mo peak at 2-3.5 Å in the r-space spectrum of Mo K-edge of MoO$_3$ nanoparticles is strong. **Figure S11b** represents the reported r-space spectra of MoO$_3$ nanoparticles reported in the literature[46]. Compared to the strong Mo-O-Mo peak of MoO$_3$ nanoparticles in 2-3.5 Å reported in the literature, the quite weak peak at 3.23 Å observed from the fresh catalyst, 0.25wt%Pd/(Co$_{0.95}$Mo$_{0.05}$)$_3$O$_4$ suggests that Mo-O-Mo is not a majority species formed in the fresh catalyst. Thus, the Mo atoms are mainly singly dispersed in the fresh catalyst.
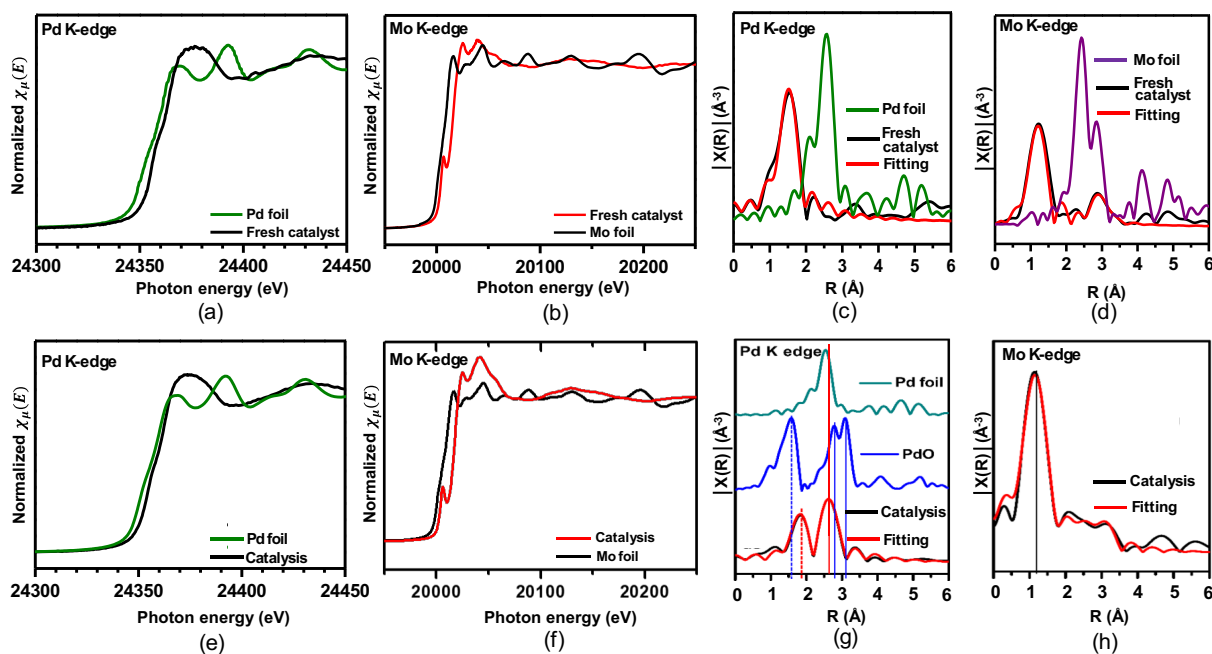
Figure 2. XANES and EXAFS studies of fresh 0.25wt%Pd/(Co$_{0.95}$Mo$_{0.05}$)$_3$O$_4$ (a-d) and 0.25wt%Pd/(Co$_{0.95}$Mo$_{0.05}$)$_3$O$_4$ during catalysis (anisole HDO at 150°C) (e-h). (a) XANES spectrum of Pd K-edge of fresh 0.25wt%Pd/(Co$_{0.95}$Mo$_{0.05}$)$_3$O$_4$ and Pd foil in ambient. **(b)** XANES spectrum of Mo K-edge of as-prepared 0.25wt%Pd/(Co$_{0.95}$Mo$_{0.05}$)$_3$O$_4$ and Mo foil in ambient. **(c)** r-space spectrum of Pd K-edge of fresh 0.25wt%Pd/(Co$_{0.95}$Mo$_{0.05}$)$_3$O$_4$ and Pd foil in ambient. **(d)** r-space spectrum of Mo K-edge of fresh 0.25wt%Pd/(Co$_{0.95}$Mo$_{0.05}$)$_3$O$_4$ and Mo foil in ambient. **(e)** XANES spectrum of Pd K-edge of 0.25wt%Pd/(Co$_{0.95}$Mo$_{0.05}$)$_3$O$_4$ during catalysis (anisole HDO at 150°C) and Pd foil in ambient. **(f)** XANES spectrum of Mo K-edge of 0.25wt%Pd/(Co$_{0.95}$Mo$_{0.05}$)$_3$O$_4$ during catalysis (anisole HDO at 150°C) and Mo foil in ambient. **(g)** r-space spectrum of Pd K-edge of 0.25wt%Pd/(Co$_{0.95}$Mo$_{0.05}$)$_3$O$_4$ during catalysis (anisole HDO at 150°C), Pd foil in ambient, and PdO in ambient. **(h)** r-space spectrum of Mo K-edge of 0.25wt%Pd/(Co$_{0.95}$Mo$_{0.05}$)$_3$O$_4$ during catalysis (anisole HDO at 150°C).

Table 1. List of parameters used to fit peaks in r-space spectra of Pd K-edge and Mo K-edge of 0.25wt%Pd/(Co$_{0.95}$Mo$_{0.05}$)$_3$O$_4$ data collected during catalysis of anisole HDO at 150°C or collected from fresh 0.25wt%Pd/(Co$_{0.95}$Mo$_{0.05}$)$_3$O$_4$ in ambient before catalysis.

Entry	Status	Path	CN	Distance (Å)	σ^2 (Å^2)
1	During catalysis at 150°C	Pd-O	2.09±0.28	2.23±0.02	0.00683
2		Pd-(O)-Co	3.17±0.51	2.92±0.02	0.00683
3		Mo-O	3.20±0.71	1.72±0.01	0.00619
4		Mo-(O)-Co	1.74±0.61	3.39±0.06	0.00619
5	Fresh catalyst in ambient at 25°C	Pd-O	3.15±1.11	2.01±0.03	0.00141
6		Mo-O	1.75±0.64	1.71±0.03	0.00387
7		Mo-(O)-Co	0.88±0.63	3.23±0.09	0.00397

The energy space spectrum of Pd K-edge of the fresh catalyst, 0.25wt%Pd/(Co$_{0.95}$Mo$_{0.05}$)$_3$O$_4$ (black spectrum in **Figure 2a**) is distinctly different from Pd foil (green spectrum in **Figure 2a**). Its r-space spectrum (black spectrum in **Figure 2c**) only has one peak at 2.01 Å, distinctly different from the peak of Pd foil (green spectrum in **Figure 2c**). The peaks of Pd-O and Pd-O-Pd of the reference sample, the well crystalized PdO nanoparticles in ambient are presented in the blue spectrum in **Figure 2g**. Compared to the spectra of the reference sample PdO nanoparticles (blue spectrum in **Figure 2g**) and another reference sample Pd foil (green spectrum in **Figure 2c**), the r-space spectrum of the fresh catalyst, 0.25wt%Pd/(Co$_{0.95}$Mo$_{0.05}$)$_3$O$_4$ (black spectrum in **Figure 2c**) does not have either the peaks of Pd-O-Pd of PdO nanoparticles or the peak of Pd-Pd of Pd foil, suggesting that Pd atoms in the fresh catalyst, 0.25wt%Pd/(Co$_{0.95}$Mo$_{0.05}$)$_3$O$_4$ are singly dispersed. The fitting to the spectrum of the fresh catalyst (red spectrum in **Figure 2c**) suggests that the Pd atoms are singly dispersed and only bond with oxygen atoms. The lack of peak of Pd-(O)-Co in the black spectrum in **Figure 2c** suggests that the singly dispersed Pd atoms of the fresh catalyst, 0.25wt%Pd/(Co$_{0.95}$Mo$_{0.05}$)$_3$O$_4$ are mainly on the surface instead of in the subsurface or in the bulk.

2.1.4 XANES, EXAFS, and AP-XPS studies of 0.25wt%Pd/(Co$_{0.95}$Mo$_{0.05}$)$_3$O$_4$ during catalysis

The coordination and chemical environments of the Mo and Pd atoms of 0.25wt%Pd/(Co$_{0.95}$Mo$_{0.05}$)$_3$O$_4$ during anisole HDO at 150°C were studied using XANES, EXAFS, and AP-XPS. The Pd K-edge spectrum of 0.25wt%Pd/(Co$_{0.95}$Mo$_{0.05}$)$_3$O$_4$ (black spectrum in **Figure 2e**) was collected during catalysis at 150°C. In terms of the r-space spectrum of the Pd K-edge of 0.25wt%Pd/5.0%Mo/Co$_3$O$_4$ during catalysis, two peaks were observed at 2.23 Å and 2.92 Å in the black spectrum in **Figure 2g**, assigned to Pd-O and Pd-(O)-Co bonds, respectively. For comparison, the r-space spectrum of Pd K-edge of the reference sample PdO nanoparticles is presented in **Figure 2g** (blue spectrum). The first peak in this blue spectrum was assigned to Pd-O bonds, and the second and third peaks were contributed from two different Pd-(O)-Pd interactions in the Pd-O-Pd units of the PdO nanoparticles.[47] Compared to the r-space spectrum of PdO nanoparticles, the lack of the two featuring peaks of Pd-O-Pd of PdO nanoparticles in the r-space spectrum of 0.25wt%Pd/5.0%Mo/Co$_3$O$_4$ during catalysis suggests that no PdO nanoparticles were formed in 0.25wt%Pd/5.0%Mo/Co$_3$O$_4$ during catalysis. The major feature of metallic Pd foil in the r-space spectrum (green spectrum in **Figure 2g**) is the peak of Pd-Pd bonds at 2.75 Å. The lack of such a Pd-Pd peak of Pd foil in the spectrum of 0.25wt%Pd/(Co$_{0.95}$Mo$_{0.05}$)$_3$O$_4$ during catalysis at 150°C indicates that no Pd metal nanoparticles were formed during catalysis at 150°C. In addition to these deductions from EXAFS, the lack of metallic Pd clsuters and PdO nanoparticles was suppported by AP-XPS studies of 0.25wt%Pd/(Co$_{0.95}$Mo$_{0.05}$)$_3$O$_4$ during catalysis at 150°C in Figure 3d3 and the ex-situ studies with HR-TEM (**Figure 1c-1e**).

Based on the black spectrum in **Figure 2g**, neither Pd-O-Pd peak of PdO nanoparticles nor Pd-Pd peak of Pd nanoparticles was observed in the r-space spectrum of $0.25wt\%Pd/(Co_{0.95}Mo_{0.05})_3O_4$ during catalysis, suggesting that the Pd atoms exist in the form of single-atom sites, Pd_1 during the catalysis at 150^oC. Coordination numbers and bond lengths around Pd_1 single atoms during catalysis were estimated through fitting the r-space spectrum of $0.25wt\%Pd/(Co_{0.95}Mo_{0.05})_3O_4$ during catalysis (red spectrum in **Figure 2g**). They are listed in entry 1-4 in **Table 1**. Based on this fitting, a Pd atom coordinates with 2.09±0.28 oxygen atoms and 3.17±0.51 cobalt atoms in its first and second shells, respectively. The low coordination numbers of a Pd_1 atom suggest that Pd atoms of $0.25wt\%Pd/(Co_{0.95}Mo_{0.05})_3O_4$ during catalysis at 150^oC are mainly on the surface of the support. The potential possibilities of fitting the r-space spectrum of Pd K-edge collected from $0.25wt\%Pd/(Co_{0.95}Mo_{0.05})_3O_4$ during catalysis at 150^oC were discussed in **Section 4.3** of the SI and later compared to these distances between Pd and Co atoms in the intermediates obtained in DFT calculations in **Section 8.3** of the SI.
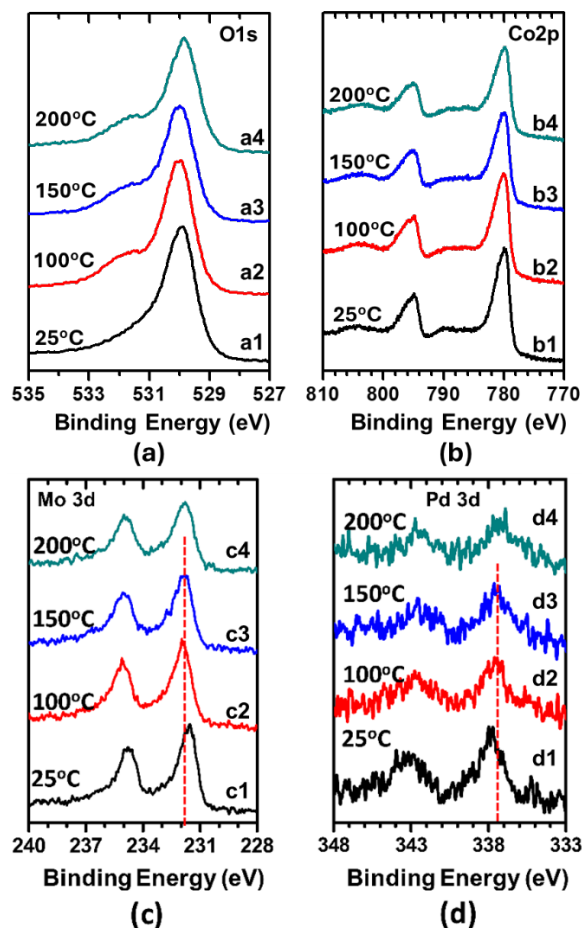
Figure 3. XPS studies of $0.25wt\%Pd/(Co_{0.95}Mo_{0.05})_3O_4$ at 25^oC (black spectra) and AP-XPS studies of $0.25wt\%Pd/(Co_{0.95}Mo_{0.05})_3O_4$ during catalysis at 100^oC (red spectra), 150^oC (blue spectra), and 200^oC (green spectra). (a) O 1s. (b) Co 2p. (c) Mo 3d. (d) Pd 3d.

The bonding of Pd with oxygen atoms was further supported by the binding energy (BE) of Pd 3d during catalysis at 150^oC tracked with AP-XPS (**Figure 3d3**). The BE of Pd $3d_{5/2}$ of $0.25wt\%Pd/(Co_{0.95}Mo_{0.05})_3O_4$ during catalysis at 150^oC, 337.2 eV, is obviously higher than those of metallic Pd or Pd-Co bimetallic nanoparticles, 335.0-335.3 eV reported in literature,[48-50] confirming that the Pd atoms of $0.25wt\%Pd/(Co_{0.95}Mo_{0.05})_3O_4$ during catalysis are cationic. This cationic nature of Pd atoms is further supported by the energy position of Pd K-edge in XANES study of $0.25wt\%Pd/(Co_{0.95}Mo_{0.05})_3O_4$ during catalysis at 150^oC (black spectrum in **Figure 2e**). The lack of palladium oxide or Pd metal nanoparticles in the HR-TEM images of

0.25wt%Pd/$(Co_{0.95}Mo_{0.05})_3O_4$ after catalysis at 150°C (**Figure 1c-1e**) supports that Pd does not exist in the form of metal oxide or metallic nanoparticles.

Compared to the coordination environment of Pd atoms in the 0.25wt%Pd/$(Co_{0.95}Mo_{0.05})_3O_4$ during catalysis at 150°C (entries 1 and 2 in **Table 1**), Pd atoms in the fresh catalytic have a different coordination environment as listed in entry 5 in **Table 1**. It suggests that the fresh catalyst was restructured by the pretreatment in 5% H_2 at 150°C and the catalysis condition at 150°C. In the following computational studies (**Section 2.7**), the structural model of the catalyst 0.25wt%Pd/$(Co_{0.95}Mo_{0.05})_3O_4$ was built on the basis of the structural parameters of 0.25wt%Pd/$(Co_{0.95}Mo_{0.05})_3O_4$ during catalysis.

The black spectrum in **Figure 2h** is the r-space spectrum of Mo K-edge of 0.25wt%Pd/$(Co_{0.95}Mo_{0.05})_3O_4$ during catalysis. In this spectrum, only a peak at 1.72 Å was observed. For MoO_3 nanoparticles reported in the literature,[46] however peaks at 2.90 Å and 3.12 Å attributed to Mo-(O)-Mo interactions in Mo-O-Mo units in addition to the Mo-O peak were simultaneously observed.[46] They are represented in **Figure S11b**. In terms of Mo foil,[26, 46] its Mo K-edge in r-space spectrum is featured by two peaks at 2-3 Å (pink spectrum in **Figure 2d**). However, the r-space spectrum of Mo K-edge of 0.25wt%Pd/$(Co_{0.95}Mo_{0.05})_3O_4$ during catalysis at 150°C does not have any peak at a R value higher than 2.0 Å (black spectrum in **Figure 2h**). It suggests that neither MoO_3 nor metallic Mo nanoparticles were formed during catalysis. The spectrum of 0.25wt%Pd/$(Co_{0.95}Mo_{0.05})_3O_4$ during catalysis (black spectrum in **Figure 2h**) was fitted into a single peak (red spectrum in **Figure 2h**). This fitting suggests that each Mo atom coordinates with 3.20±0.71 oxygen atoms in the first shell and 1.74±0.61 Co atoms in the second shell (entry 3 and 4 in **Table 1**). The lack of formation of Mo metal or MoO_3 nanoparticles on 0.25wt%Pd/$(Co_{0.95}Mo_{0.05})_3O_4$ during catalysis is supported by the surface sensitive AP-XPS

studies during catalysis (**Figure 3c3**) since the observed binding energy of Mo 3d of 0.25wt%Pd/$(Co_{0.95}Mo_{0.05})_3O_4$ during catalysis, 231.8 eV, is obviously higher than that of metallic Mo reported in literature,[48] but lower than that of MoO_3.[51-53] In addition, in-situ XANES spectra of the Mo K-edge of 0.25wt%Pd/$(Co_{0.95}Mo_{0.05})_3O_4$ during catalysis (red spectrum in **Figure 2f**) show that Mo atoms are cationic, consistent with its coordination with oxygen atoms deduced from in situ studies of EXAFS and AP-XPS.

Compared to the coordination environment of Mo atoms in 0.25wt%Pd/$(Co_{0.95}Mo_{0.05})_3O_4$ during catalysis (entries 3-4 in **Table 1**), the Mo atoms of the fresh catalyst are in a different coordination environment (entry 6-7 in **Table 1**). Thus, obviously the coordinating environment of Mo atoms was restructured by the pretreatment in 5% H_2 at 150°C and the following catalysis at 150°C. This restructuring made a Mo atom directly bond with 3.20±0.71 oxygen atoms and 1.74±0.61 cobalt atoms in the first and second coordination shells. This structural parameter was used in building structural model of 0.25wt%Pd/$(Co_{0.95}Mo_{0.05})_3O_4$ during catalysis for exploring catalytic mechanism of anisole HDO in **Section 2.7**.

2.2 Preparation and characterization of $(Co_{0.95}Mo_{0.05})_3O_4$ and 0.25wt%Pd/Co_3O_4

Compared to 0.25wt%Pd/$(Co_{0.95}Mo_{0.05})_3O_4$ containing two types of single-atom sites, Mo_1 and Pd_1, the catalyst $(Co_{0.95}Mo_{0.05})_3O_4$ containing only one type of single-atom sites Mo_1 and the catalyst 0.25wt%Pd/Co_3O_4 containing only one type of single-atom sites Pd_1 were prepared as described in **Sections S1.2 and S1.4**, respectively. The r-space spectrum of the Mo K-edge of $(Co_{0.95}Mo_{0.05})_3O_4$ (**Figure S12**) shows that the Mo atoms are singly dispersed in $(Co_{0.95}Mo_{0.05})_3O_4$ during anisole HDO at 150 °C and coordinate with 3.20±0.28 oxygen atoms on average, similar to Mo atoms in 0.25wt%Pd/$(Co_{0.95}Mo_{0.05})_3O_4$ during catalysis. The in-situ

XANES spectrum shows that the Mo atoms in $(Co_{0.95}Mo_{0.05})_3O_4$ are cationic (**Figure S13**). Similar to the single dispersion of Pd atoms in $0.25wt\%Pd/(Co_{0.95}Mo_{0.05})_3O_4$, the Pd atoms of the $0.25wt\%Pd/Co_3O_4$ after catalysis for HDO anisole at 150^oC are still singly dispersed on Co_3O_4 (**Figure S7**). In the following sections, the $(Co_{0.95}Mo_{0.05})_3O_4$, $0.25wt\%Pd/Co_3O_4$, and $0.25wt\%Pd/(Co_{0.95}Mo_{0.05})_3O_4$ catalysts are designated as Mo_1/Co_3O_4, Pd_1/Co_3O_4 and Mo_1+Pd_1/Co_3O_4, respectively for convenience.

2.3 Realization of active and selective catalysis with teamed Pd_1 and Mo_1 sites at low temperature
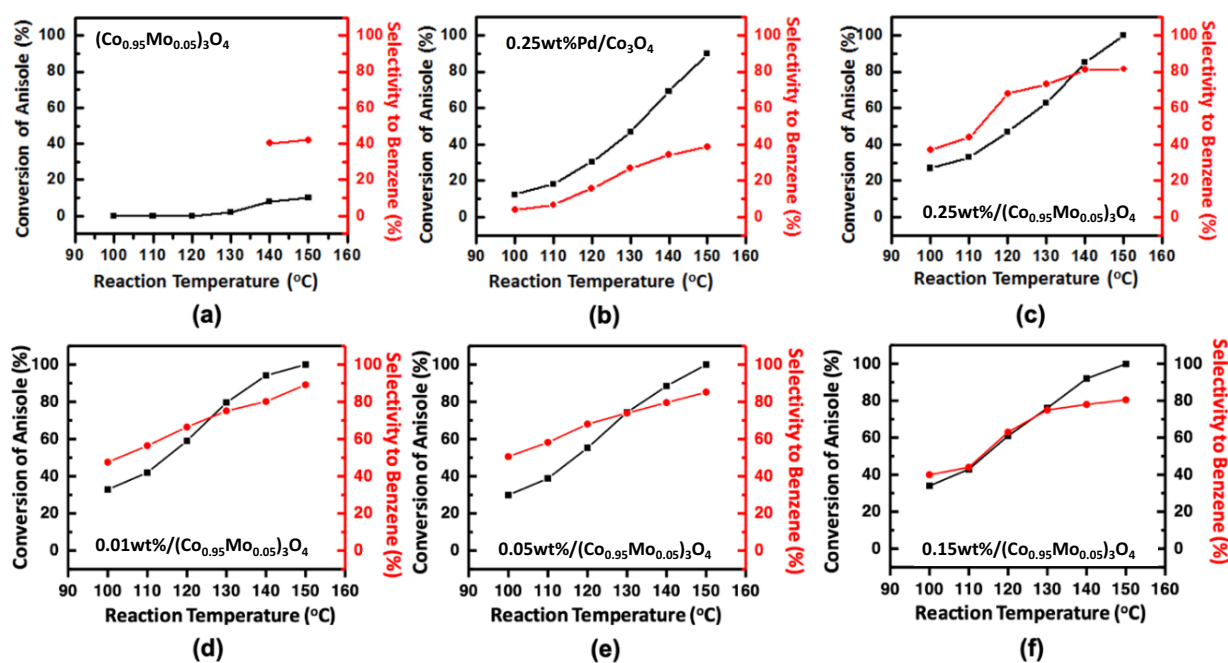
Figure 4. Catalytic activity and selectivity for benzene formation through anisole hydrodeoxygenation (HDO) on catalysts. (a) Catalytic performances of 50 mg of $(Co_{0.95}Mo_{0.05})_3O_4$ (Mo_1/Co_3O_4). (b) Catalytic performances of 50 mg of $0.25wt\%Pd/Co_3O_4$ (Pd_1/Co_3O_4). (c) Catalytic performances of 50 mg of $0.25wt\%Pd/(Co_{0.95}Mo_{0.05})_3O_4$ (Mo_1+Pd_1/Co_3O_4). (d-f) Catalytic performances of x wt%Pd/$(Co_{0.95}Mo_{0.05})_3O_4$ with increased amount of Pd (x) from 0.01wt%, 0.05wt% to 0.15wt%. In each measurement of catalytic performance, 50 mg of a catalyst was mixed with 300 mg of purified quartz**.** In all catalytic measurements, the anisole vapor was delivered to the catalyst bed through the flowing H_2. For delivering anisole vapor, 25 mL/min H_2 (99.99%) was introduced to a sealed bottle containing about 10 ml 99.9% anisole; the liquid anisole in the bottle remained at room temperature by keeping the bottle in a room-temperature water bath without additional heating or cooling.

The catalytic activity and selectivity of anisole HDO on the three different catalysts, Mo_1/Co_3O_4, Pd_1/Co_3O_4, and Mo_1+Pd_1/Co_3O_4 were measured in a fixed-bed flow reactor under the catalytic condition as described in **Section S6**. As shown in **Figure 4a**, 50 mg of $(Co_{0.95}Mo_{0.05})_3O_4$ is nearly inactive for the conversion of anisole in 100-130°C; The conversion of anisole on 50 mg $(Co_{0.95}Mo_{0.05})_3O_4$ at 150°C is <10% with a selectivity of only 40% for producing benzene. 50 mg of Pd_1/Co_3O_4 exhibits a larger conversion of anisole, 68% at 140°C and 88% at 150°C, but the selectivity for benzene remains quite low (35% at 140°C and 40% at 150°C) (**Figure 4b**). The main side-reaction channel is the hydrogenation of the phenyl ring of anisole.

In comparison, the catalyst with teamed single-atom sites, Mo_1+Pd_1/Co_3O_4, exhibits 87% conversion of anisole at 140°C and 98% at 150 °C (**Figure 4c**). The selectivity for benzene through anisole HDO at 140 °C and 150 °C on Mo_1+Pd_1/Co_3O_4 (**Figure 4c**) are 81% and 83%, respectively, obviously higher than that on Mo_1/Co_3O_4 (**Figure 4a**) and Pd_1/Co_3O_4 (**Figure 4b**) by at least 40%-45%. These parallel studies clearly show that teaming the two types of single-atom sites, Pd_1 and Mo_1, on Co_3O_4 to form Mo_1+Pd_1/Co_3O_4 allows the benzene production through anisole HDO of anisole to be efficiently and selectively performed at a temperature as low as 100-150°C. The yields of benzene from 50 mg of Mo_1+Pd_1/Co_3O_4 at 150°C, 83%, and at 140°C, 72%, are much higher than the total yield (39.2%) of 50 mg Pd_1/Co_3O_4 (35%) and 50 mg of Mo_1/Co_3O_4 (4.2%) at 150°C, clearly justifying the team effect of Pd_1 and Mo_1 sites on Co_3O_4 in this low-temperature range. The high low-temperature activity of the Mo_1+Pd_1/Co_3O_4 for anisole HDO contrasts the absence of activity in producing benzene through anisole HDO on Pd metal nanoparticles of 0.50wt%Pt/SiO$_2$ (**Figure S19**) at 300°C or lower, and on MoO$_3$ nanoparticles at a temperature 200°C or lower (**Figure S20**).[13] It justifies the hypothesis that a

low temperature catalysis, unable to be reached on a classical metal or oxide nanoparticle catalyst, can be realized by teaming two sets of single-atom sites on a support.

The teaming effect of Pd_1- and Mo_1-based sites on the support, Co_3O_4 was clearly confirmed by the evaluation of catalytic performance of a physical mixture of 50 mg 0.25%Pd/Co_3O_4 (Pd_1/Co_3O_4) and 50 mg $(Mo_{0.05}Co_{0.95})_3O_4$ (Mo_1/Co_3O_4). As listed in **Table S5**, the yield of benzene on the physical mixture in Column 3 is always lower than that on 50 mg 0.25wt%$Pd/(Co_{0.95}Mo_{0.05})_3O_4$ [Mo_1+Pd_1/Co_3O_4] in Column 2 in the temperature range of 120-150°C by 11.4%-28.5% (Column 4. These differences listed in **Table S5** clearly supported the team effect of Pd_1 and Mo_1 on anisole HDO at these catalysis temperatures.

In terms of the catalytic stability of 0.25wt%$Pd/(Co_{0.95}Mo_{0.05})_3O_4$ [Mo_1+Pd_1/Co_3O_4], we performed time-stream experiments for 0.25wt%$/(Co_{0.95}Mo_{0.05})_3O_4$ at 140°C for 96 hours. As shown in **Figure S21**, the yield of benzene remains about 72% for at least 96 hours. In addition, we also tested the reusability of the catalysts by repeating the ramping up and cooling down. The yield for benzene remained nearly constant in the first four cycles (**Figure S22**).

2.4 Hydrogen spillover on the support of teamed Pd_1-based and Mo_1-based sites of 0.25wt%$Pd/(Co_{0.95}Mo_{0.05})_3O_4$

The potential influence of the loading of Pd atoms on the catalytic performance of anisole HDO was explored through systematic studies under the same catalytic condition as used in **Figure 4**. 0.01wt%$Pd/(Co_{0.95}Mo_{0.05})_3O_4$, 0.05wt%$Pd/(Co_{0.95}Mo_{0.05})_3O_4$, and 0.15wt%$Pd/(Co_{0.95}Mo_{0.05})_3O_4$ were prepared with the same method as 0.25wt%$Pd/(Co_{0.95}Mo_{0.05})_3O_4$ described in **Section S1.3**. The actual loadings of Pd and Mo are listed in **Table S2**. These four catalysts with different loadings of Pd [x wt%$Pd/(Co_{0.95}Mo_{0.05})_3O_4$] exhibit very similar conversions of anisole and selectivity for benzene

at 150°C (**Figures 4c-4f**). It suggests that the amount of Pd_1 sites on $(Co_{0.95}Mo_{0.05})_3O_4$ is not critical for kinetics. It also indicates that the step performed on Pd atoms, dissociation of H_2 as we will show in the computational studies (**Section 2.7**), can proceed even with an actual loading of Pd as low as 0.003at% (entry 1 in **Table S2**). This suggests a low activation barrier for dissociating H_2 on Pd_1 site and a high spillover rate of H atoms on the support, Co_3O_4.

The hydrogen spillover effect of Co_3O_4 was confirmed by the following experiment. We measured catalytic performance of a physical mixture of 50 mg 0.25%Pd/Co_3O_4 (Pd_1/Co_3O_4) and 50 mg $(Mo_{0.05}Co_{0.95})_3O_4$ (Mo_1/Co_3O_4) to compare to the catalytic performance of 50 mg 0.25%Pd/Co_3O_4 (Pd_1/Co_3O_4) or that of 50 mg $(Mo_{0.05}Co_{0.95})_3O_4$ (Mo_1/Co_3O_4). Column 2, 3, and 5 in **Table S4** list the yield of 50 mg 0.25wt%Pd/Co_3O_4 (Pd_1/Co_3O_4), yield of 50 mg $(Mo_{0.05}Co_{0.95})_3O_4$ (Mo_1/Co_3O_4), and the yield of the physical mixture of 50 mg 0.25%Pd/Co_3O_4 (Pd_1/Co_3O_4) and 50 mg $(Mo_{0.05}Co_{0.95})_3O_4$ (Mo_1/Co_3O_4) in 110-150°C, respectively. Clearly, the yield of benzene generated from the physical mixture of 50 mg 0.25%Pd/Co_3O_4 (Pd_1/Co_3O_4) and 50 mg $(Mo_{0.05}Co_{0.95})_3O_4$ (Mo_1/Co_3O_4) in Column 5 in **Table S4** is obviously higher than the sum (Column 4) of the yield from 50 mg 0.25%Pd/Co_3O_4 (Pd_1/Co_3O_4) and that from 50 mg $(Mo_{0.05}Co_{0.95})_3O_4$ (Mo_1/Co_3O_4). Column 6 in **Table S4** lists the difference between the yield of the mixture (Column 5) and the sum of the yields of the two catalysts (Column 4). This comparison shows that H atoms can readily spillover on surfaces of Co_3O_4 which is the support of Mo_1/Co_3O_4, Pd_1/Co_3O_4, Mo_1+Pd_1/Co_3O_4. It confirmed the role of the support Co_3O_4 in H spillover.
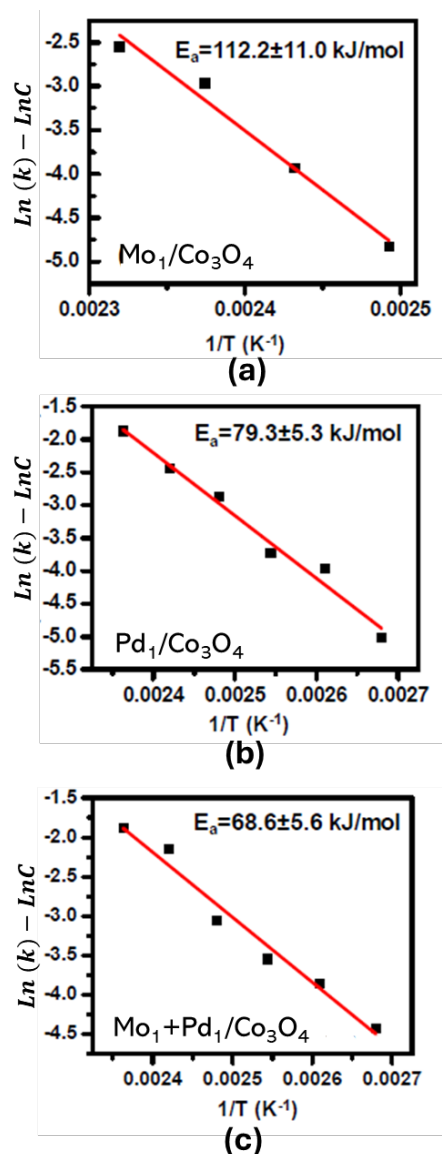
Figure 5. **Kinetics studies of anisole HDO on (a) $(Co_{0.95}Mo_{0.05})_3O_4$, (Mo_1/Co_3O_4), (b) 0.25wt%Pd/Co$_3$O$_4$ (Pd_1/Co_3O_4), and (c) 0.25wt%Pd/$(Co_{0.95}Mo_{0.05})_3O_4$ (Mo_1+Pd_1/Co_3O_4) in 100-150°C for measuring apparent activation energies.** In these kinetics studies, 5 mg catalyst was mixed with 100 mg quartz and conversions of anisole are always lower than 15%.

2.5 Kinetic studies of the team effect of Pd_1 and Mo_1 single-atom sites for anisole HDO

To check whether the observed differences in catalytic performance among Mo_1+Pd_1/Co_3O_4 (**Figure 4c**), Pd_1/Co_3O_4 (**Figure 4b**), and Mo_1/Co_3O_4 (**Figure 4a**), and the

difference listed in **Table S5**, are intrinsic or not, the kinetics studies of anisole HDO on the three catalysts was performed in the temperature range of 100-150°C, where the conversions of anisole were always kept $\leq 10\%$ (See **Section S6.2**). **Figure 5** shows the plots of $Ln(k) - LnC$ as a function of $\frac{1}{T}$. The rate constant, k can be calculated with the equation (1): $k = \frac{Q_{anisole\ flowing\ into\ reactor} \times Y_{benzene}}{N_{surface\ site} \times [A]^a [B]^b}$. The definition of Q, Y, N, [A], and [B] can be found in the **SI**, in **Section S6.2**. When the conversion is $\leq 10\%$, rate constant, k is nearly linearly proportional to the yield of benzene through the equation (2), $k = Y_{Benzene} \times C$ since Q, Y, and N are constant, and the slight variations of [A] and [B] does not obviously influence the rate constant, k in the narrow temperature range (100-150°C) as described in **Section S6.2**. Then, there is a correlation, $LnY_{Benzene} = Ln(k) - LnC$. Thus, the plot of $Ln\ (Y_{Benzene})$ as a function of $\frac{1}{T}$ has the same slope as the Arrhenius plot where $Ln\ (k)$ is plotted as a function of $\frac{1}{T}$. Based on the slopes of these plots in **Figure 5a** for Mo_1/Co_3O_4, **Figure 5b** for Pd_1/Co_3O_4, and **Figure 5c** for Mo_1+Pd_1/Co_3O_4, the apparent activation energies for producing benzene through anisole HDO on Mo_1/Co_3O_4, Pd_1/Co_3O_4, and Mo_1+Pd_1/Co_3O_4 are calculated to be 112±11 kJ/mol, 79±5 kJ/mol, and 69±6 kJ/mol, respectively. Thus, the apparent activation barrier on Mo_1+Pd_1/Co_3O_4, 69±6 kJ/mol is lower than that of Pd_1/Co_3O_4 having only Pd_1 single-atom sites, 79±5 kJ/mol, and markedly lower than that of Mo_1/Co_3O_4 having only Mo_1 single-atom sites, 112±11 kJ/mol.
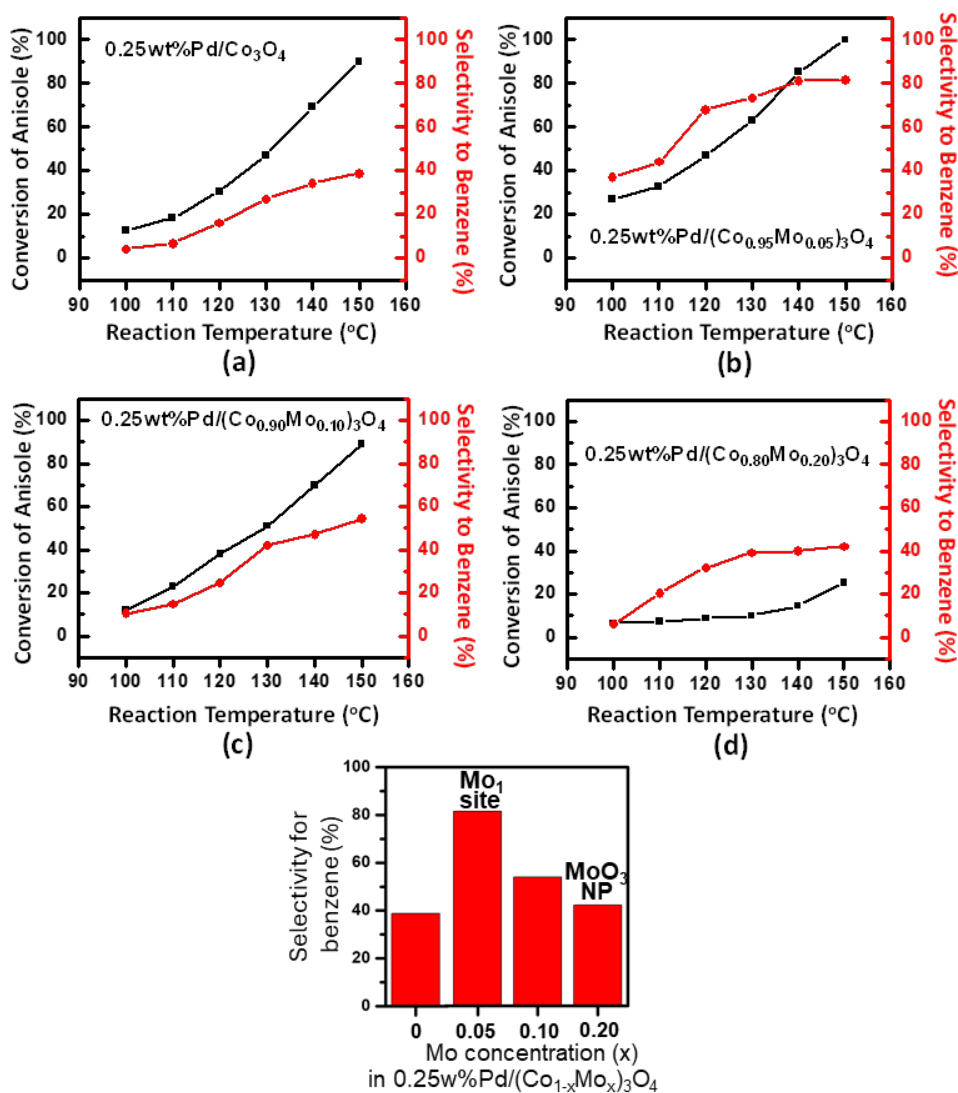
Figure 6. Catalytic activity and selectivity for the anisole HDO on the 0.25wt%Pd/(Co$_{1-x}$Mo$_x$)$_3$O$_4$. Catalytic performances of (a) 50 mg of 0.25wt%Pd/Co$_3$O$_4$, Pd$_1$/Co$_3$O$_4$, (b) 50 mg of 0.25wt%Pd/(Co$_{0.95}$Mo$_{0.05}$)$_3$O$_4$, Mo$_1$+Pd$_1$/Co$_3$O$_4$. (c) 50 mg of 0.25wt%Pd/(Co$_{0.90}$Mo$_{0.10}$)$_3$O$_4$, (d) 50 mg of 0.25wt%Pd/(Co$_{0.80}$Mo$_{0.80}$)$_3$O$_4$, and (e) Selectivity for producing benzene at 150°C as a function of the amount of Mo integrated in the synthesis of (Co$_{1-x}$Mo$_x$)$_3$O$_4$. In each measurement, 50 mg of catalyst was mixed with 300 mg of purified quartz. In all catalytic measurements, 25 mL/min H$_2$ (99.99%) was introduced to a sealed bottle containing about 10 ml anisole (99.9%); The liquid anisole in the bottle was maintained at room temperature by keeping the bottle in a water bath without additional heating or cooling; the anisole vapor was delivered to the catalyst bed with the flowing H$_2$.

It is found that the Mo$_1$ sites play a significant role. By including Mo$_1$ single-atom sites, the selectivity for benzene at 150°C is increased from 38% on Pd$_1$/Co$_3$O$_4$ in **Figure 6a** to 83% on Mo$_1$+Pd$_1$/Co$_3$O$_4$ (**Figure 6b**). Notably, the selectivity decreases from 83% to 56% at 150°C

along increase of the loading of Mo from 5% to 10% (**Figure 6b versus 6c**). When Mo loading is further increased from 10% to 20%, the selectivity for benzene on $0.25wt\%Pd/(Co_{0.80}Mo_{0.20})_3O_4$ decreases from 56% to 42% at 150^oC (**Figure 6c versus 6d**). The selectivity for benzene on $0.25wt\%Pd/(Co_{0.80}Mo_{0.20})_3O_4$, 42% in **Figure 6d** is very similar to that on $0.25wt\%Pd/Co_3O_4$, 38% in **Figure 6a**. **Figure 6e** presents a volcano-like evolution of selectivity for producing benzene through anisole HDO with a maximum for a Mo concentration of ~5%. This evolution suggests that Mo_1 single-atom sites instead of MoO_3 nanoparticle played a significant role in promoting the catalytic selectivity for benzene in anisole HDO. XRD shows that MoO_3 nanoparticles were formed in the $0.25wt\%Pd/(Co_{0.80}Mo_{0.20})_3O_4$, evidenced by the observation of the shoulder at 29.8^o in **Figure 1a6**. Thus, obviously the MoO_3 nanoparticles are not active for producing benzene through anisole HDO.

2.6 Restructuring of $0.25wt\%Pd/(Co_{0.95}Mo_{0.05})_3O_4$ at relatively high temperature and decayed catalytic performance in HDO

Catalytic performance of 35 mg of $0.25wt\%Pd/(Co_{0.95}Mo_{0.05})_3O_4$ was evaluated in the temperature range of $150-300^oC$ (**Figure S18**). The conversion of anisole on 35 mg catalyst at 150^oC is 75% which is consistent with the conversion of anisole (98%) obtained on 50 mg of this catalyst at 150^oC (**Figure 4c**). Unfortunately, selectivity for producing benzene largely decreased along the elevation of catalysis temperature from 150^oC to 300^oC. Notably, the selectivity for producing benzene is near zero at $250-300^oC$ although the conversions of anisole at these temperatures are high. Based on AP-XPS studies, Pd atoms of $0.25wt\%Pd/(Co_{0.95}Mo_{0.05})_3O_4$ were partially reduced at 250^oC and completely reduced to metallic Pd at 300^oC (**Figure S17b**) while Mo remained at an oxidizing state (**Figure S17a**). The correlation between the measured

low catalytic selectivity for benzene through anisole HDO at 200-300°C (**Figure S18**) and the reduction of cationic Pd to metallic Pd in this temperature range (**Figure S17b**) shows that Pd metal nanoparticles are not active for production of benzene through anisole HDO at a temperature of ≤300°C.

Our 0.25wt%Pd/(Co$_{0.95}$Mo$_{0.05}$)$_3$O$_4$ active for HDO at 100-150°C consists of Co$_3$O$_4$ with anchored Pd$_1$ and Mo$_1$ single atom sites. It is distinctly different from the Pd-Mo bimetallic nanoparticle catalyst supported on the inert support, SiO$_2$ reported in literature.[13] On the reported Pd-Mo NPs/SiO$_2$ catalyst,[13] Mo and Pd formed Pd-Mo bimetallic nanoparticles at 150°C-300°C. The nature of the bimetallic catalysis on Pd-Mo bimetallic nanoparticles supported on SiO$_2$ is distinctly different from the team effect of two sets of single-atom sites, Mo$_1$ and Pd$_1$ on Co$_3$O$_4$ of 0.25wt%Pd/(Co$_{0.95}$Mo$_{0.05}$)$_3$O$_4$. Another difference is that the catalysis temperature for producing benzene through anisole HDO. On Pd-Mo NPs/SiO$_2$ it is active in 150°C-300°C but here 0.25wt%Pd/(Co$_{0.95}$Mo$_{0.05}$)$_3$O$_4$ is highly active for producing benzene in 100-150°C.

2.7 Molecular mechanism of catalysis on teamed single-atom sites at low temperature

To understand the roles of Pd$_1$ and Mo$_1$ single sites in low-temperature catalysis, the reaction pathways for anisole HDO over each type of site of the catalyst were investigated with DFT, together with the surface molecular diffusion process on the surface of the support between these sites.

2.7.1 Structure of the Co$_3$O$_4$(111) surface and the anchored Mo$_1$ and Pd$_1$ sites

We optimized the geometries of Pd_1 and Mo_1 sites. Due to the low surface atomic fractions of both Mo_1 and Pd_1 in this catalyst, we modeled the two sites separately anchored on Co_3O_4. The (111) surface of Co_3O_4 was chosen to represent the support since the (111) is the most prevalently exposed termination of spent catalysts as determined by HR-TEM (**Figure 1c-1e**).
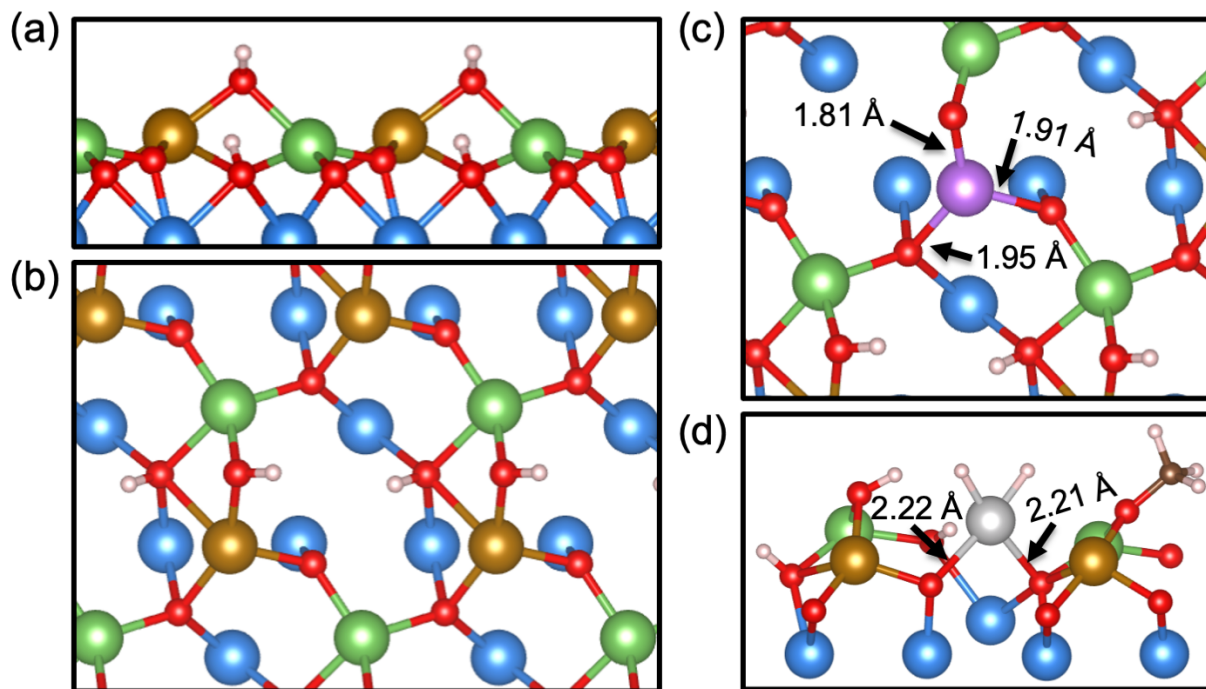
Figure 7. Optimized structures of the hydroxylated $Co_3O_4(111)$ surface and the anchored Mo_1 and Pd_1 surface sites. (a) Side view of the structure of the hydroxylated $Co_3O_4(111)$ surface in equilibrium with the gas environment during steady state reaction. The surface is Co-enriched and hydroxylated, terminated with 7.11 Co/nm^2 and 7.11 OH/nm^2. Oxidized $Co_3O_4(111)$ films are terminated by O (red) and Co (green). Co (gold) atoms are added to simulate surface reduction without phase-change to CoO in the near-surface layers. (b) Top view of the hydroxylated $Co_3O_4(111)$ surface. (c) Top view of the optimized Mo_1 site constructed by substituting one of the gold-coloured Co cations on the hydroxylated surface with Mo and removing one unit of H_2O. (d) Side view of the optimized Pd_1 site constructed by adsorbing one unit of PdH_2 and substituting a nearby OH group by OCH_3 on hydroxylated Co_3O_4.

Under catalytic conditions, the $Co_3O_4(111)$ surface was found from computational exploration of surface terminations to be heavily hydroxylated (7.11 OH/nm^2, **Figure 7**).[54] As such, we explored several configurations of a grafted Pd_1 site and the geometry of a substituted

Mo$_1$ site based on stoichiometry (see **Section S8.2**). In these conditions, the Pd$_1$ active site is calculated to be formally in a (+2) oxidation state (see **Section S8.3** for formal charge assignment), coordinated to two hydrides and two surface O atoms in a square planar arrangement (**Figure 7d**). For the Mo$_1$ site, although the mono-oxo-molybdenum site is the most stable configuration, we selected a 3-fold coordinated substituted Mo site as the starting point because it is only mildly metastable by 0.26 eV under low anisole conversion, and the highly coordinated Mo sites are rather inert as shown in studies on the activation of CH$_4$ over MoO$_3$/SiO$_2$.[55] This Mo$_1$ site in **Figure 7c** was generated by replacing one surface Co with Mo and removing one lattice OH plus one H from another adjacent OH (see **Section S8.2**).

2.7.2 Reaction mechanism of anisole HDO over Pd$_1$/Co$_3$O$_4$
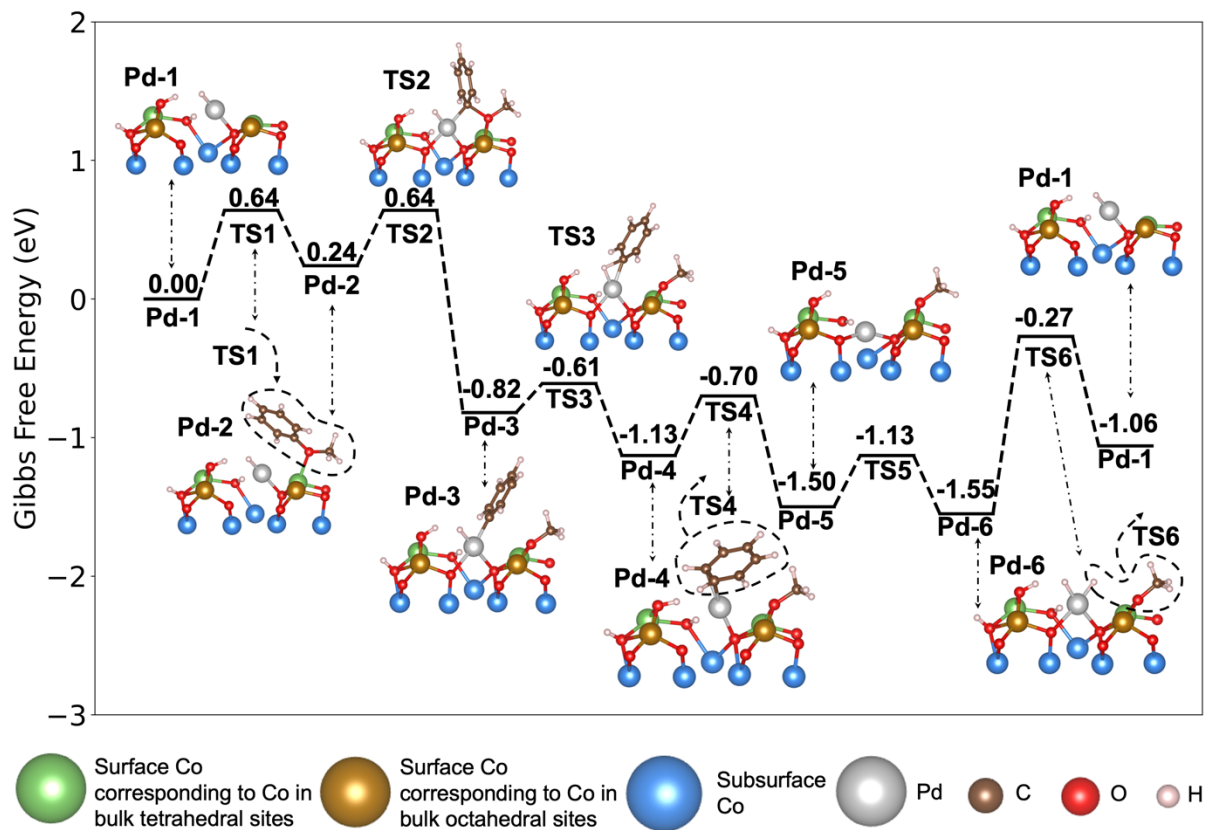
Figure 8. Gibbs free energy pathway for anisole HDO over the Pd₁ site shows that the methanol formation controls the energetic span. All structures in the reaction pathway are listed in **Figure S25** and more structural details of the intermediates are shown in **Figure S26.** Anisole HDO over only the Pd₁ site takes advantage of a single O vacancy near the Pd₁. The energetic span of the reaction mechanism is 1.28 eV, between the PdH₂ intermediate (Pd-6) and the transition state for the desorption of methanol (TS6).

Next, to compare the anisole HDO activity on different catalysts, we first examined the reaction mechanism over the Pd₁ site alone (**Figure 8**). We found the anisole HDO to occur at the interface between the Pd₁H₂ site and the hydroxylated Co₃O₄(111) support (**Figure 8**). Similar to some reported reaction mechanisms on metal oxide-containing catalysts, the mechanism over Pd₁ requires the participation of an O vacancy near to the Pd₁.[56-58] We started the cycle not at the most stable and abundant Pd₁H₂ structure, but with a Pd₁ site (Pd₁H₁, Pd-1 in **Figure 8**) containing a single hydride (H) ligand and an O vacancy (Oᵥ) in the vicinity of the Pd₁ active site. The Pd₁H₁ and a nearby O vacancy are generated from the recombination of a H atom of Pd₁H₂ and a hydroxyl or alkoxyl species on the support (Pd-1 on **Figure 8**). Formally, the formed Pd₁H₁ complex is closest to a combined oxidation state of (-1) (see **Section S8.3**). A more stable Pd₁H₂ site where the Pd cation is in a +2 formal oxidation state is formed later in the catalytic cycle.

In the first step, the oxygen atom of an anisole molecule is adsorbed on the O vacancy near Pd₁H₁ (structure Pd-2 in **Figure 8**). The activation of Gibbs free energy of this step from Pd-1 to Pd-2 through TS-1 (0.64 eV) is estimated from the kinetic theory of gases (see **Section S9.1;** a similar analysis has been presented in reference [59]). By crossing a 0.40 eV barrier from Pd-2 to Pd-3 through TS2 in **Figure 8**, the adsorbed anisole dissociates by breaking its C-O bond between C₆H₅ and OCH₃ (C_ring-O), to form a phenyl (C₆H₅) ligand on Pd₁H₁ and a methoxy (OCH₃) group on the Co atoms surrounding the O vacancy near Pd₁ (Pd-3 in **Figure 8**). The key C_ring-O cleavage hence occurs at Pd₁-oxide interface; in other words, the support assists the Pd₁

cation to facilitate the C_{ring}-O cleavage at the transition state (TS2 in **Figure 8**). The Pd_1 center is oxidized from Pd_1H_1 (-1) to Pd (+2) in this largely exothermic step (ΔG=-1.06 eV). In comparison, the unwanted hydrogenation of the aromatic ring of anisole by the Pd_1H_1 species is an endothermic process with a reaction energy of 0.57 eV, which is less energetically favorable (**Figure S28 and Section S8.4**).

On the other hand, the intramolecular hydrogenation of the formed C_6H_5 group by the H ligand of Pd_1H_1 to form a benzene molecule in the step from Pd-3 to Pd-4 through TS3 is expectedly easy, requiring only 0.22 eV (**Figure 8**), reducing the Pd (+2) center to Pd (0). After the desorption of benzene in the step from Pd-4 to Pd-5 through TS4, a bare Pd_1 is formed in Pd-5. Then, H_2 replenishes the bare Pd_1 site to form PdH_2 in Pd-6, reoxidizing the bare Pd (0) center Pd (+2) in Pd-6. The formation of PdH_2 proceeds by crossing a small barrier of 0.37 eV from Pd-5 to TS5. Since no potential energy barrier was found for the dissociation of H_2, the free energy barrier for this step is purely comprised of entropy losses corresponding to a collision theory adsorption rate. Clearly, as anticipated, H_2 dissociation is easy on the Pd_1 site of Pd-5 and does not appear to be a rate determining step at all. The formed Pd_1H_2 in Pd-6 is the most stable square-planar Pd_1 active site mentioned above. Finally, one H ligand reacts with the adjacent OCH_3 on the Co atom in the step from Pd-6 to Pd-1 through TS6 to form methanol and restore the original (-1) Pd_1H_1 site of Pd-1, closing the catalytic cycle on the Pd_1/Co_3O_4 surface. No potential energy barrier was found for the readsorption of methanol; thus, the additional entropy contribution to the desorption barrier was estimated using collision theory. Notably, the formation and desorption of methanol from Pd_1H_2 and a nearby OCH_3 group in Pd-6 through TS6 requires a rather large Gibbs free energy barrier of 1.28 eV (**Figure 8**). This is the catalytic cycle of anisole HDO on Pd_1/Co_3O_4, a catalyst with only one set of single-atom sites, Pd_1.

In the mechanism described above, anisole does not initially adsorb on the Pd_1H_1 site, but the phenyl fragment formed from C_{ring}-O dissociation binds to Pd_1 through the radical C (Pd-2 to Pd-3 in **Figure 8**). This is consistent with the weak chemisorption of anisole on the Pd_1 site even on the bare Pd_1 site without a H ligand in Pd-5. Additional calculations found that anisole could chemisorb on Pd_1 without a H ligand (Pd-5) through its phenyl ring; however, this chemisorption is endergonic by 0.15 eV under reaction conditions (**Figure S29**). The chemisorption of anisole on Pd_1 of Pd-5 is not energetically preferred since the chemisorption of H_2 on Pd_1 of Pd-5 is slightly exothermic (ΔG=-0.05 eV).
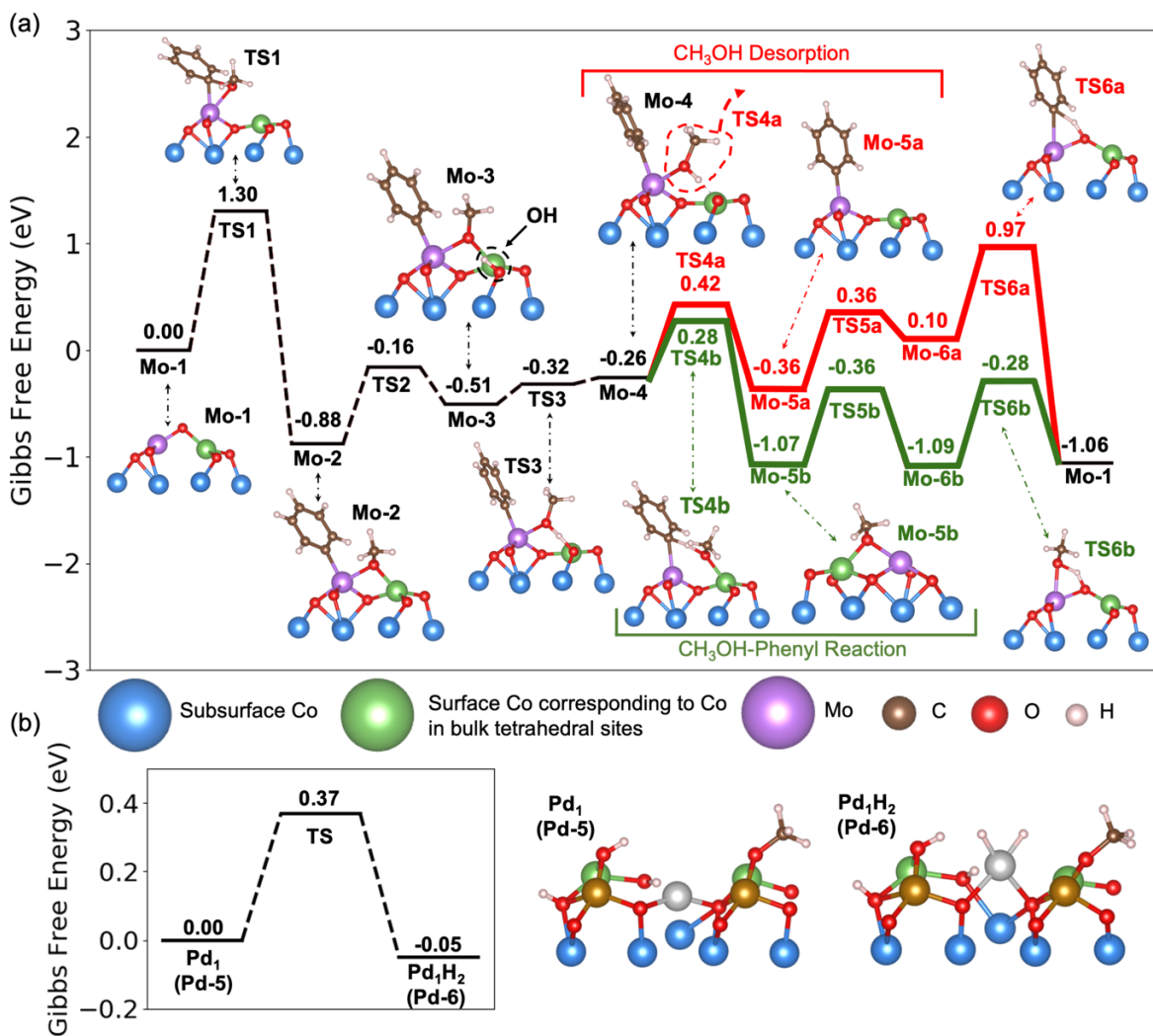
Figure 9. Gibbs free energy pathway for anisole HDO over the Mo$_1$+Pd$_1$ site. (a) Anisole HDO over the Mo$_1$ site assisted by H spillover formed on Pd$_1$ site. All structures in the reaction pathway are listed in **Figure S27**. The energetic span of the reaction mechanism is 1.34 eV under low conversion (1%), between the state Mo-6b and the transition state (TS1) for the dissociation of the anisole molecule. After the dissociation of anisole, a methanol molecule is formed first by reacting OCH$_3$ with a surface H. The methanol molecule can desorb (pathway in red) or donate its H to the phenyl group and form benzene. This sub-pathway is shown in red, designated as methanol-first sub-pathway. Alternatively, upon dissociation of anisole, a benzene molecule can form first to desorb and then a methanol molecule forms to desorb. This sub-pathway is shown in green, designated as benzene-first sub-pathway. (b) Gibbs free energy barrier for the dissociation of molecular H$_2$ on the Pd$_1$ site and the structure of the relevant intermediates.

2.7.3 Reaction mechanism of anisole HDO over Mo$_1$+Pd$_1$/Co$_3$O$_4$

2.7.3.1 Dissociation of C$_{ring}$-O of anisole on Mo$_1$ site

We explored next the anisole HDO over the teamed single-atom Pd$_1$+Mo$_1$/Co$_3$O$_4$ catalyst, where reactivity on the Mo$_1$ site is assisted by the Pd$_1$ site for H$_2$ dissociation and the support for H spillover (**Figure 9**). Since this undercoordinated Mo$_1$ site in Mo-1 in **Figure 9** appears to have very little steric hindrance, we found that the C$_{ring}$-O bond is cleaved through oxidative addition. In the transition state (TS1), the C$_{ring}$-O bond is stretched to 1.76 Å and forms a triangle with the Mo$_1$ center. This step produces in Mo-2 a C$_6$H$_5$ fragment whose carbon atom binds to the Mo$_1$ center and an OCH$_3$ fragment whose O atom bridges over the Mo$_1$ center (purple) and its neighboring Co (green). In combination, this step raises the formal oxidation state of Mo$_1$ in Mo-1 from +3 to +4 (see **Section S8.3**). The Gibbs free energy barrier to break the C$_{ring}$-O bond in this oxidative addition step is 1.30 eV (TS1), accounting for the loss of gas-phase entropy upon adsorption. Here again the Co atoms on the support play a role, although not in the C-O bond cleavage (TS1) but rather in the stabilization of the product (Mo-2). To continue the reaction, the C$_6$H$_5$ and OCH$_3$ fragments must be hydrogenated.

2.7.3.2 Dissociation of H$_2$ on the Pd$_1$ site and spillover on the Co$_3$O$_4$ support

The dissociation of H_2 over Pd_1, from Pd-5 to Pd-6, only requires crossing a Gibbs free energy barrier of 0.37 eV, through TS5 (**Figure 8 or 9b**). Other sites present on the catalyst such as Co and Mo_1 were also considered for the dissociation of H_2, but they were found to be much less active than the Pd_1 site (**Figures S30 and S31 and Section S8.5**). Accounting for the translational and rotational degrees of freedom, the dissociation of H_2 on the hydroxylated $Co_3O_4(111)$ substrate is estimated to have an activation barrier of 1.62 eV Gibbs free energy (**Figure S30**). The activation barrier over the Mo_1 site is even as high as 2.39 eV (**Figures S31**). The high activation barriers for dissociating molecular H_2 on Mo_1 and Co forces H_2 dissociation to occur on the Pd_1 site of Mo_1+Pd_1/Co_3O_4 (**Figure 9b**), while the hydroxylated $Co_3O_4(111)$ substrate acts as a H adsorbate reservoir, where surface H is in quasi-equilibrated with H_2 gas. This explains why Mo_1/Co_3O_4 is hardly active for anisole HDO in **Figure 4a** since the activation barrier for H_2 dissociation on Mo_1 and Co is high.

Spillover of H across the Co_3O_4 support surface occurs through a Grotthuss type motion involving metastable water intermediates and the Co_3O_4 surface itself as an electron reservoir.[60] The H spillover event on $Co_3O_4(111)$ presents an electronic energy barrier of 0.63 eV (**Figure S32**) which is markedly lower than the 1.30 eV barrier for cleaving the C_{ring}-O bond at Mo_1 in the step from Mo-1 to Mo-2 (**Figure 9a**). In our pathway in **Figure 9a**, the whole process of H_2 adsorption and spillover is lumped in a single effective step from Mo-2 to Mo-3 through TS2, where a proton and electron are brought close to the Mo_1 site (forming Mo-3), with a net Gibbs free energy barrier of 0.72 eV from Mo-2 to TS2 and a Gibbs free energy of reaction of +0.37 eV from Mo-2 to Mo-3. A detailed description of the H spillover mechanism on the catalyst surface is presented in **Figure S32** and **Section S8.5**.

2.7.3.3 Two possible sub-pathways for producing benzene and methanol on Mo$_1$ sites

After the cleavage of C$_{ring}$-O of anisole, the OCH$_3$ species of Mo-4 can first desorb as a methanol molecule through the methanol-first sub-pathway of Mo-4→Mo-5a→Mo-6a to Mo-1. Alternatively, the C$_6$H$_5$ ligand of Mo-4 can desorb first as a benzene molecule through the benzene-first sub-pathway of Mo-4→Mo-5b→Mo-6b→Mo-1. We first explored the steps in the methanol-first sub-pathway in red in **Figure 9a**. From the collision theory rate of adsorption/desorption, methanol can be desorbed by crossing a 0.68 eV Gibbs free energy barrier (Mo-4 to TS4a **in Figure 9a**), then one more H may be transferred to bind to the O atom bridging between Mo and Co of Mo-5a, forming Mo-6a. This H atom will react with C$_6$H$_5$ to form benzene in the step of Mo-6a to Mo-1. In the step of Mo-5a to Mo-6a, the Mo center is reduced from +4 in Mo-5a to +3 in Mo-6. In the step from Mo-6a to Mo-1, the bridging OH group reacts with the C$_6$H$_5$ ligand to form a free benzene molecule by crossing a 0.87 eV Gibbs free energy barrier, restoring the Mo$_1$ active site (Mo-1, most-right side of **Figure 9a**). This step (Mo-6a to Mo-1) couples a proton transferred from the OH group and an electron from the substrate. In this sub-pathway (red in **Figure 9a**), CH$_3$OH first desorbs and then benzene is formed and desorbs from the catalyst surface.

We next explored the benzene-first sub-pathway (in green) starting from Mo-4 in **Figure 9a**. The OCH$_3$ formed through TS3 can rotate and react with the C$_6$H$_5$ ligand to form a benzene molecule and an OCH$_3$ group bridging over Mo$_1$ and Co atoms (TS4b). In other words, the methoxy group acts as a relay for transferring the proton from the oxide surface to the phenyl fragment. This step requires a 0.54 eV barrier relative to Mo-4, which is slightly smaller than the desorption barrier of methanol (0.68 eV from Mo-4 to TS4a in **Figure 9a**) in the alternative methanol-first sub-pathway. In this step from Mo-4 to Mo-5b, the Mo$_1$ center is formally reduced

from +4 to +3. The near-linear configuration of the C_{ring}, H, and O atoms in this transition state (TS4b) resembles that for σ bond metathesis.[61] Due to the relatively high thermodynamic stability of the bridging OCH_3 group in Mo-5b, the formation and desorption of a benzene molecule in the step from Mo-4 to Mo-5b is much more exergonic (ΔG=-0.82 eV) than the desorption of a methanol molecule in the step from Mo-4 to Mo-5a (ΔG=-0.11 eV). To close the catalytic cycle, one more H is brought to Mo_1 of Mo-6b by spillover, by which the bridging OCH_3 group (Mo-6b) is re-hydrogenated through crossing a 0.81 eV barrier (TS6b) to form methanol which then desorbs, restoring the Mo-1 site. Interestingly, the net free energy barrier to hydrogenate OCH_3 on the Mo_1 site of Mo-6b (0.81 eV, from Mo-6b to TS-6b in Figure 9a) is much smaller than the barrier of hydrogenating OCH_3 in the step from Pd-6 to Pd-1 through TS6 on Pd_1 of Pd_1/Co_3O_4 (1.28 eV from Pd-6 to TS6 in **Figure 8**).

Overall, compared to the methanol-first sub-pathway (red in **Figure 9a**), this alternative sub-pathway (green) of first desorbing benzene and then CH_3OH, is kinetically preferred as the methoxy group acting as a relay lowers the barrier for the formation of benzene. In addition to this pathway over the Mo_1 site formed by substituting a Co atom, the reactivity of a grafted Mo_1 site (IS-1 in **Figure S33**) was also explored (**Figure S33 and Section S8.6 in SI**). Compared to the substituted Mo_1 site, the grafted Mo_1 site is much more prone to poisoning by OCH_3, which strongly binds atop the Mo_1 site (**Figure S33**). Although the free energy barrier to cleave the C_{ring}-O bond of anisole (IS-1 to TS1 in **Figure S33**) is 1.24 eV, the free energy change of methanol recombination (IS-4b to IS-6 in **Figure S33**) is 0.65 eV, resulting in a free energy span of 1.90 eV in **Figure S33**, higher than that of the substituted Mo_1 site (**Figure 9a**), making the grafted Mo_1 site less reactive. Considering that the actual catalyst could present a distribution of

Mo$_1$ active sites, we expect the fraction of substituted Mo$_1$ sites to be responsible for the observed reactivity.

2.8 Theoretical assessments of anisole HDO kinetics over Pd$_1$/Co$_3$O$_4$ and Pd$_1$/Mo$_1$/Co$_3$O$_4$

2.8.1 Energetic span assessment of the reaction kinetics
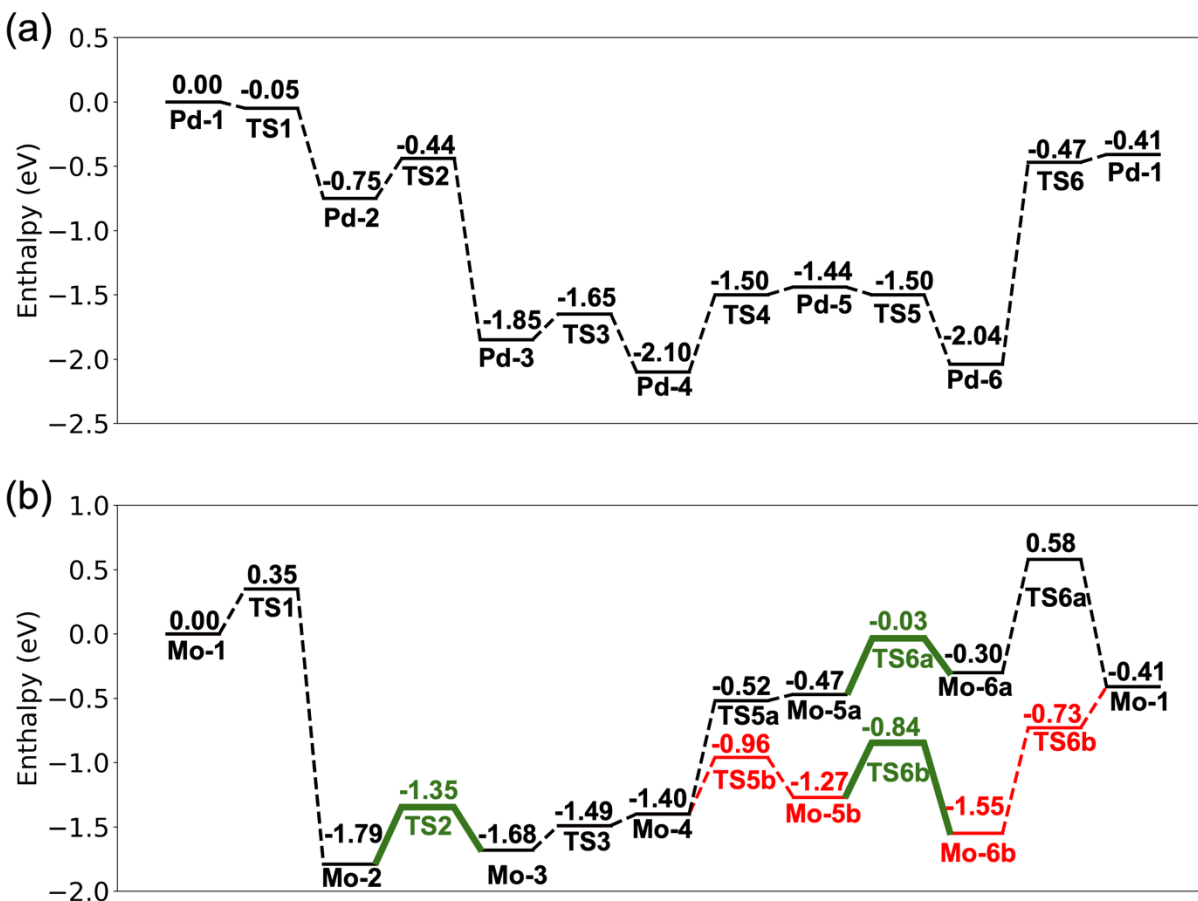
Figure 10. Enthalpy pathways for the HDO of anisole (a) over Pd$_1$ and (b) over Mo$_1$ assisted by H spillover.

With the Gibbs free energy of all reactants, products, IS, and TS in the reaction defined, we model the kinetics of anisole HDO and compare them to the experimental measurements, beginning with an energetic span analysis of the reaction pathways. Since the energetic span model is derived from the analytical solution for the TOF of single-site catalytic reactions at a

specific steady state conversion, it is appropriate for analysing the single-site HDO mechanisms developed in this work (**Figure 8 and 9**).[62-64]

For the reaction over Pd_1 only at 1% anisole conversion, we find two possible TOF-determining intermediates (TDIs), the bare Pd (Pd-5) and PdH_2 (Pd-6), but one TOF-determining transition state (TDTS), corresponding to the desorption of methanol. All relevant Gibbs free energy spans (ΔG_{span}) are listed in **Table S11**. Here, Pd-6 and the TS of methanol desorption are the most dominant TDI and TDTS. Between this pair of states, we find a free energy span ΔG_{span} of 1.28 eV (**Figure 8**) and an enthalpy span (ΔH_{span}) of 1.57 eV (**Figure 10a**). For the HDO reaction over Mo_1 assisted by H spillover, we find that Mo-1, Mo-5b and Mo-6b are possible candidates for the TDI, while TS1 is the sole candidate for the TOF-determining transition state (TDTS) (**Figure 9a**). Mo-6b and TS1 are the most dominant TDI and TDTS, where ΔG_{span} span is 1.34 eV and ΔH_{span} is 1.49 eV (**Figure 10**).

With the relevant ΔG_{span} and ΔH_{span} in hand, we can calculate the reaction rates and apparent activation energies. From the general form of the analytical rate in ref [62], we see that the rate of reaction should be:

$$r = \frac{k_B T}{h} \frac{\theta_{k,0}}{\sum_{i,j} \exp\left(\frac{\Delta G_{span,IS-i/TS-j}}{RT}\right)} \quad (1)$$

Where $\theta_{k,0}$ denotes the total surface coverage of active site k, and i and j denote the i-th IS and j-th TS occurring over site k. The apparent activation energy of a rate law in the above form is:

$$E_{a,app} = RT + \sum_{i,j} p_{i,j} \Delta H_{span,IS-i/TS-j} \quad (2)$$

Where $p_{i,j}$ is the Boltzmann-like weight of the free energy span between IS-i and TS-j:

$$p_{i,j} = \frac{\exp\left(\frac{\Delta G_{span,IS-i/TS-j}}{RT}\right)}{\sum_{i,j} \exp\left(\frac{\Delta G_{span,IS-i/TS-j}}{RT}\right)} \quad (3)$$

We note that equation (2) is a free-energy-span-specific variation of that of Mao and Campbell, which relates the degree of rate control to apparent activation energy in a microkinetic simulation.[65] Using the equations (1-3) and the spans in **Table S11**, we find the turnover frequency over only the Pd_1 sites to be $2.29 \cdot 10^{-1}$ min^{-1} and the apparent activation energy to be 1.49 eV at 150 °C. For the HDO reaction mechanism over Mo_1 assisted by H spillover (**Figure 9**), we find its TOF to be $3.44 \cdot 10^{-2}$ min^{-1} and the apparent activation energy to be 1.24 eV at 150 °C. Given that the Mo_1 sites outnumber Pd_1 by more than 10-fold (**Table S6**), these calculations show that the $Mo_1 + Pd_1/Co_3O_4$ is kinetically favourable over Pd_1/Co_3O_4, confirming the team effect of Mo_1 and Pd_1 on Co_3O_4 in anisole HDO. On the other hand, as the Gibbs free energy barriers of H_2 dissociation over the $Co_3O_4(111)$ substrate and the Mo_1 site are 1.62 eV and 2.39 eV **(Figure S30 and S31)**, the Mo_1/Co_3O_4 catalyst is obviously less active than the Pd_1/Co_3O_4 catalyst.

As it is important to assess the impact of the accuracy of the electronic structure description on the calculated rates, we tested the sensitivity of the predicted reactivity to the effective Hubbard U (U_{eff}) values for Co and Mo. As shown in **Table S12**, we found that the transition state and intermediates have opposing sensitivity to the value of U_{eff}, resulting in a small net difference on the energy spans of the catalytic cycle. Although the free energy span of the reaction over Mo_1 increases slightly when a smaller value of U_{eff} is used for either or both Co and Mo (2.0 eV and 3.0 eV respectively), the overall activity of the catalyst still benefits from the presence of H spilled over from Pd_1.

2.8.2 Microkinetic modeling of the reaction kinetics and analysis
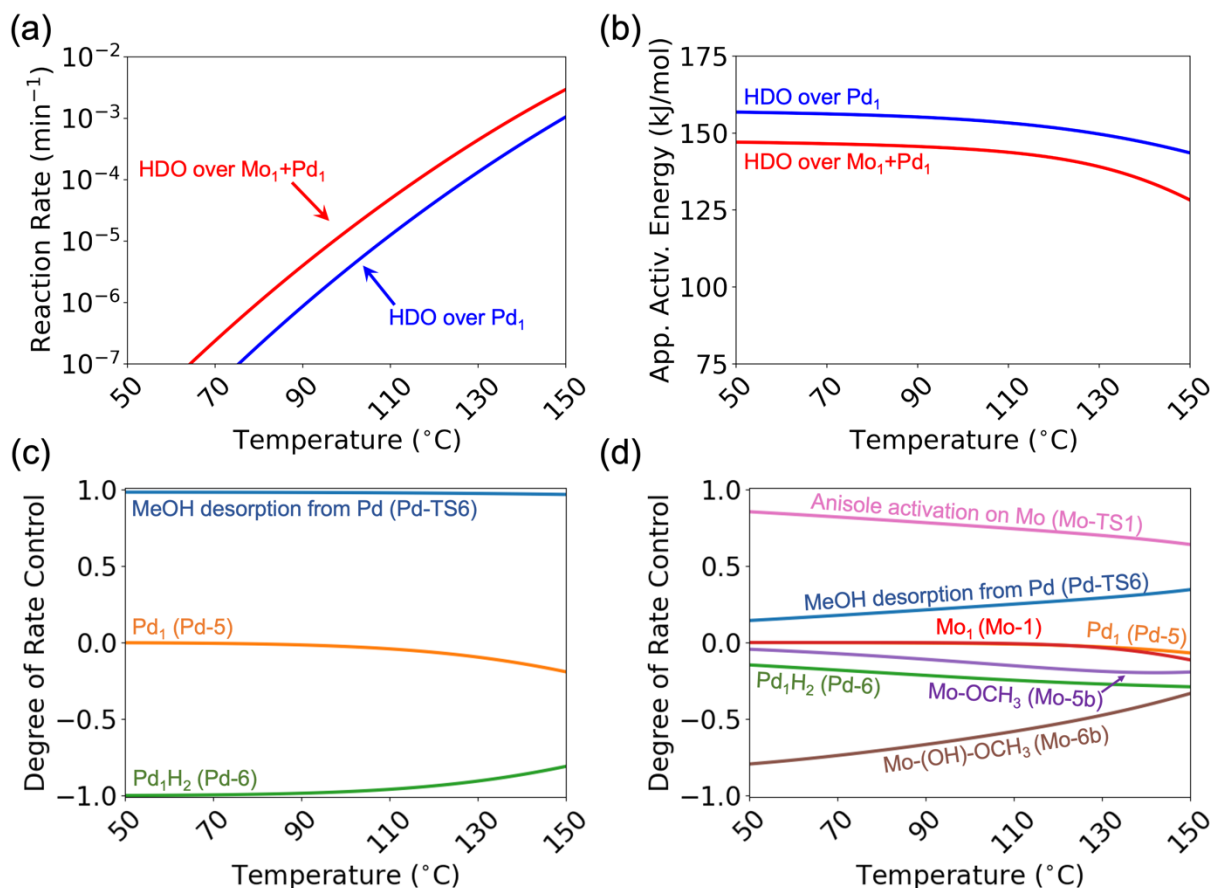
Figure 11. Microkinetic simulations showing that the teamed Mo$_1$+Pd$_1$ catalyst is more active than Pd$_1$ for anisole HDO at 50-150°C. (a) Calculated reactions rate as a function of catalysis temperature show that the teamed Mo$_1$+Pd$_1$/Co$_3$O$_4$ catalyst is more active than the Pd$_1$/Co$_3$O$_4$ single-site catalyst in the temperature range of 50-150°C. (b) Calculated apparent activation energy as a function of catalysis temperature show that the activation barrier for HDO over Mo$_1$ assisted by H spillover (Mo$_1$+Pd$_1$/Co$_3$O$_4$) is smaller than that over only Pd$_1$ (Pd$_1$/Co$_3$O$_4$) in this temperature range as well. (c) Degree of rate control (DRC) of key intermediates and transition states in anisole HDO over Pd$_1$/Co$_3$O$_4$. (d) DRC of key intermediates in anisole HDO over Mo$_1$+Pd$_1$/Co$_3$O$_4$. DRC analyses show that the decrease of the apparent activation energy with temperature is due to the depletion of surface intermediates.

To solidify the link between the DFT-calculated energy profiles and the catalysis experiments, we developed microkinetic models for the proposed reaction mechanisms over Mo$_1$+Pd$_1$/Co$_3$O$_4$ and Pd$_1$/Co$_3$O$_4$, to quantify the rates of anisole HDO (**Sections S9.3**).[62, 66, 67] These simulations show that the Mo$_1$ site of the Pd$_1$+Mo$_1$/Co$_3$O$_4$ catalyst is the main contributor to the overall catalytic activity along with the assistance of the Pd$_1$ site to activate H$_2$ molecules. The rate of anisole HDO over Mo$_1$+Pd$_1$/Co$_3$O$_4$ was found to be consistently higher than that over

Pd$_1$/Co$_3$O$_4$ in the temperature range 50-150 °C (**Figure 11a**). As temperature rises, the apparent activation energies of the HDO reaction over both Mo$_1$ assisted by H spillover and Pd$_1$ decrease as the coverage of reactive intermediates decrease (**Figure 11b**). These findings are consistent with our free energy span analysis presented above in **subsection 2.8.1**.

For further analysis, we computed the degree of rate control (DRC) of key intermediates and transition states in the reaction mechanisms. As shown in **Figure 11c**, in the anisole HDO over only Pd$_1$, the desorption of methanol is the sole rate-controlling TS (Pd-TS6, blue), while the bare Pd$_1$ species (Pd-5, orange) and the PdH$_2$ species (Pd-6, green) are the rate-controlling intermediates. The coverage of hydrides on Pd$_1$ gradually decreases with temperature, resulting in an increasing DRC of PdH$_2$ and a lowering apparent activation energy (**Figure 11b**). These results agree with those from our energetic span analysis, where we found the TS of the desorption of methanol to be the sole TDTS and the bare Pd$_1$ site and PdH$_2$ to be the TDIs (**Figures 8 and 10**).

On the other hand, for the teamed Pd$_1$+Mo$_1$ catalyst, the dissociation of anisole over Mo$_1$ is the main rate-controlling TS through the temperature range 50-150 °C (Mo-TS1, pink, **Figure 11d**). On the other hand, the bridging methoxy with a nearby OH [Mo-(OH)-OCH$_3$ (Mo-6b), brown] is the main rate-controlling intermediate. The importance of this intermediate is reflected in the high apparent activation energy at 50 °C. As temperature increases, the importance of Mo-6b decreases, which results in a decrease of the apparent activation energy with temperature (**Figure 11b**). Similar to the case of anisole HDO over only Pd$_1$, these results also agree with those from our energetic span analysis, where we found the dissociation of anisole to be the sole TDTS and the Mo$_1$ with a bridging methoxy (Mo-6b) to be the main TDI.

2.8.3 Comparison to experimental findings

The apparent activation energy $E_a(app)$ over Mo_1+Pd_1/Co_3O_4 predicted from computational studies is lower than that over Pd_1/Co_3O_4 as shown in Figure 11b, which qualitative agrees with the experimental measurements (**Figure 5c versus 5b**). Further, the configurations of the Mo_1 and Pd_1 sites on Mo_1+Pd_1/Co_3O_4 (Mo-6b with a bridging OCH_3 in **Figure 9a** and Pd-6 with two adsorbed H^- in **Figure 9b**) found during steady state reaction also agree with the coordination environment of Mo_1 and Pd_1 sites experimentally measured by the in-situ EXAFS studies (entries 1-4 in **Table 1**). Our in-situ EXAFS studies of Pd_1+Mo_1/Co_3O_4 catalyst show that the Mo atoms are coordinated to 3.20 ± 0.71 oxygen atoms, while the Pd atoms are coordinated to 2.09 ± 0.28 oxygen atoms (**Table 1**). Finally, the link between the active site coverage and catalyst reactivity is also revealed. In the catalytic tests, we found that when both Mo_1 and Pd_1 sites are present on the Co_3O_4 support, the catalyst reactivity is not sensitive to the amount of Pd_1 sites (**Figure 4c-f**). This is well rationalized by computational studies since H_2 dissociation (Pd-TS5) is not a rate-determining step. As long as Pd_1 sites are present on the same catalyst particle to generate surface H, the Mo_1 sites will have H to perform the reaction.

The quantitative differences between the calculated apparent activation energies over the Pd_1 and Pd_1+Mo_1 catalysts and the experimentally measured ones could be due to the gas composition used in the microkinetic model. Although the HDO reaction over the Pd_1 site alone does not depend on the partial pressure of methanol, a lower H_2 partial pressure would make the intermediate Pd-5 become the rate-controlling one, resulting in a lower activation energy. Thus, a lower H_2 partial pressure can make the barrier predicted from computational studies better agree with the measured apparent active energy on Pd_1/Co_3O_4. For instance, using an H_2 partial pressure of ~10 kPa instead of ~100 kPa would destabilize the intermediate Pd-6 by ~0.08 eV,

making Pd-5 the most abundant intermediate and bringing the apparent activation energy on Pd_1/Co_3O_4 closer to the experimentally measured one.

On the other hand, the reaction over the Mo_1 site, when assisted by H spillover, is less prone to poisoning by the methanol product than the reaction over Pd_1 alone, as seen in the free energy profiles shown in **Figures 8 and 9a.** This difference implies that a more inlet-like gas composition (even lower than 1% anisole conversion) would result in a lower apparent activation energy and better agreement with experiment. For instance, lowering anisole conversion, and thereby the partial pressure of the product methanol, by an order of magnitude will destabilize intermediates Mo-5b and Mo-6b by ~0.08 eV, making Mo-1 the most abundant intermediate and drastically lowering the apparent activation energy. Similarly, considering the reaction over the grafted Mo_1 site (**Figure S33**), a type of site different from the substituted Mo_1 site (Mo-1 in **Figure 9a**), we are aware that a more inlet-like gas composition could improve its reactivity by shrinking the energetic span; however, the grafted Mo_1 site will still be less reactive than the substituted Mo_1 site. This shift will also decrease the predicted Mo-O coordination number during steady state reaction, bringing it closer to that found the EXAFS measurements.

3. Conclusion

In summary, we have demonstrated that low-temperature catalysis can be realized by teaming two different single-atom sites which can temporally simultaneously but spatially separately activate two reactants A and B of a reaction [A+B→target product(s)] where an ordinary metal or oxide nanoparticle catalyst cannot. The catalyst consisting of teamed single-atom sites, Mo_1+Pd_1/Co_3O_4 was synthesized through two consecutive preparation steps. The Mo_1+Pd_1/Co_3O_4 catalyst is highly active and selective in producing benzene through anisole

HDO at 150°C while supported metal Pd or MoO$_3$ nanoparticle catalysts are inactive at this temperature. The teamed Mo$_1$+Pd$_1$/Co$_3$O$_4$ catalyst is also more active and more selective than the Pd$_1$/Co$_3$O$_4$ and Mo$_1$/Co$_3$O$_4$ catalysts since Mo$_1$/Co$_3$O$_4$ is not active and only Pd$_1$/Co$_3$O$_4$ shows some activity but low selectivity for producing benzene through anisole HDO.

Computational studies uncovered the Gibbs free energy pathways of anisole HDO on the dual site catalyst, Mo$_1$+Pd$_1$/Co$_3$O$_4$, and single site catalysts, Pd$_1$/Co$_3$O$_4$ and Mo$_1$/Co$_3$O$_4$. For the teamed single-atom site catalyst, Pd$_1$ activates H$_2$ with a free energy barrier of only 0.37 eV while Mo$_1$ cleaves the C$_{ring}$-O bond of anisole. The hydrogenation of phenyl to form benzene on the Mo$_1$ center is assisted by the methoxy fragment which acts as relay for the H transfer. The Co$_3$O$_4$ support is inactive for anisole HDO by itself but participates in the catalysis of the teamed Pd$_1$ and Mo$_1$ sites by facilitating H spillover. In turn, the hydrogenation of OCH$_3$ to form CH$_3$OH could be performed on a Mo$_1$ site with only a net free energy barrier of 0.81 eV instead of 1.28 eV over Pd$_1$. Energetic span analysis and microkinetic models built from the proposed reaction mechanisms found that the Mo$_1$+Pd$_1$/Co$_3$O$_4$ catalyst has both a higher activity and lower apparent activation energy than the Pd$_1$/Co$_3$O$_4$ catalyst.

The combined experiments and theoretical modelling therefore show that for a catalytic reaction involving multiple bond activations, several single cation sites can be efficient teamed together, with coupling via intermediate spill-over on the support, to catalyze the reaction at low temperature where traditional nanoparticle catalysts are not active. This study opens avenues for the customized design of highly efficient catalysts.

Supporting Information:

The Supporting Information is available free of charge at of charge at https://pubs.acs.org/doi/xxxx.

SI #1: Experimental methods for catalyst synthesis, ex-situ XRD, TEM, XPS, and BET characterizations, in-situ AP-XPS, in-situ XANES, and in-situ EXAFS characterizations, measurements of catalytic performance, kinetic measurements, calculations of Pd/Co atomic ratio, computational methods for DFT calculations and kinetic modeling, geometry of intermediates, and transition states in the reaction pathways over the Pd_1 site, H_2 dissociation and spillover, and alternative anisole HDO pathway. (pdf)

SI #2: Geometry of intermediates and transition states in the reaction pathways over the Pd_1 site and the substituted Mo_1 site. (zip)

Author Contributions

YT, GY, SZ, and YL made equal contributions to this work.

Acknowledgements

References

1.   Resasco, J.; Christopher, P., Atomically Dispersed Pt-group Catalysts: Reactivity, Uniformity, Structural Evolution, and Paths to Increased Functionality. *J. Phys. Chem. Lett.* **2020,** *11* (23), 10114-10123.
2.   Pang, S. H.; Schoenbaum, C. A.; Schwartz, D. K.; Medlin, J. W., Directing reaction pathways by catalyst active-site selection using self-assembled monolayers. *Nat. Commun.* **2013,** *4* (1), 2448.
3.   Cargnello, M.; Doan-Nguyen, V. V. T.; Gordon, T. R.; Diaz, R. E.; Stach, E. A.; Gorte, R. J.; Fornasiero, P.; Murray, C. B., Control of Metal Nanocrystal Size Reveals Metal-Support Interface Role for Ceria Catalysts. *Science* **2013,** *341* (6147), 771-773.
4.   Serna, P.; Gates, B. C., Molecular Metal Catalysts on Supports: Organometallic Chemistry Meets Surface Science. *Acc. Chem. Res.* **2014,** *47* (8), 2612-2620.
5.   Resasco, J.; Yang, F.; Mou, T.; Wang, B.; Christopher, P.; Resasco, D. E., Relationship between Atomic Scale Structure and Reactivity of Pt Catalysts: Hydrodeoxygenation of m-Cresol over Isolated Pt Cations and Clusters. *ACS Catal.* **2020,** *10* (1), 595-603.
6.   Zhang, Z.; Tian, J.; Lu, Y.; Yang, S.; Jiang, D.; Huang, W.; Li, Y.; Hong, J.; Hoffman, A. S.; Bare, S. R.; Engelhard, M. H.; Datye, A. K.; Wang, Y., Memory-dictated dynamics of single-atom Pt on CeO2 for CO oxidation. *Nat. Commun.* **2023,** *14* (1), 2664.
7.   Liu, L.; Corma, A., Metal catalysts for heterogeneous catalysis: from single atoms to nanoclusters and nanoparticles. *Chem. Rev.* **2018,** *118* (10), 4981-5079.
8.   Yang, X.-F.; Wang, A.; Qiao, B.; Li, J.; Liu, J.; Zhang, T., Single-Atom Catalysts: A New Frontier in Heterogeneous Catalysis. *Acc. Chem. Res.* **2013,** *46* (8), 1740-1748.
9.   Tonini, D.; Schrijvers, D.; Nessi, S.; Garcia-Gutierrez, P.; Giuntoli, J., Carbon footprint of plastic from biomass and recycled feedstock: methodological insights. *Int. J. Life Cycle Assess.* **2021,** *26* (2), 221-237.
10.   He, M.; Sun, Y.; Han, B., Green Carbon Science: Efficient Carbon Resource Processing, Utilization, and Recycling towards Carbon Neutrality. *Angew. Chem. Int. Ed.* **2022,** *61* (15), e202112835.
11.   Li, K. L.; Wang, R. J.; Chen, J. X., Hydrodeoxygenation of Anisole over Silica-Supported Ni2P, MoP, and NiMoP Catalysts. *Energy & Fuels* **2011,** *25* (3), 854-863.
12.   Sakoda, K.; Yamaguchi, S.; Mitsudome, T.; Mizugaki, T., Selective Hydrodeoxygenation of Esters to Unsymmetrical Ethers over a Zirconium Oxide-Supported Pt–Mo Catalyst. *JACS Au* **2022,** *2* (3), 665-672.
13.   Liu, X.; Zhang, S.; Zhao, H.; Lin, H.; Xu, K.; Xu, Y.; Tan, L.; Wu, L.; Tang, Y., In-situ studies on the synergistic effect of Pd-Mo bimetallic catalyst for anisole hydrodeoxygenation. *Mol. Catal.* **2022,** *530*, 112591.

14.   González-Borja, M. Á.; Resasco, D. E., Anisole and Guaiacol Hydrodeoxygenation over Monolithic Pt-Sn Catalysts. *Energy & Fuels* **2011,** *25* (9), 4155-4162.

15.   Zhu, X. L.; Lobban, L. L.; Mallinson, R. G.; Resasco, D. E., Bifunctional transalkylation and hydrodeoxygenation of anisole over a Pt/HBeta catalyst. *J. Catal.* **2011,** *281* (1), 21-29.

16.   Loricera, C. V.; Pawelec, B.; Infantes-Molina, A.; Alvarez-Galvan, M. C.; Huirache-Acuña, R.; Nava, R.; Fierro, J. L. G., Hydrogenolysis of anisole over mesoporous sulfided CoMoW/SBA-15(16) catalysts. *Catal. Today* **2011,** *172* (1), 103-110.

17.   Runnebaum, R. C.; Lobo-Lapidus, R. J.; Nimmanwudipong, T.; Block, D. E.; Gates, B. C., Conversion of Anisole Catalyzed by Platinum Supported on Alumina: The Reaction Network. *Energy & Fuels* **2011,** *25* (10), 4776-4785.

18.   Runnebaum, R. C.; Nimmanwudipong, T.; Block, D. E.; Gates, B. C., Catalytic Conversion of Anisole: Evidence of Oxygen Removal in Reactions with Hydrogen. *Catal. Lett.* **2011,** *141* (6), 817-820.

19.   Deutsch, K. L.; Shanks, B. H., Hydrodeoxygenation of lignin model compounds over a copper chromite catalyst. *Appl. Catal. A* **2012,** *447*, 144-150.

20.   Lee, W. S.; Wang, Z. S.; Wu, R. J.; Bhan, A., Selective vapor-phase hydrodeoxygenation of anisole to benzene on molybdenum carbide catalysts. *J. Catal.* **2014,** *319*, 44-53.

21.   Saidi, M.; Samimi, F.; Karimipourfard, D.; Nimmanwudipong, T.; Gates, B. C.; Rahimpour, M. R., Upgrading of lignin-derived bio-oils by catalytic hydrodeoxygenation. *Energy Environ. Sci.* **2014,** *7* (1), 103-129.

22.   Jin, S. H.; Xiao, Z. H.; Li, C.; Chen, X.; Wang, L.; Xing, J. C.; Li, W. Z.; Liang, C. H., Catalytic hydrodeoxygenation of anisole as lignin model compound over supported nickel catalysts. *Catal. Today* **2014,** *234*, 125-132.

23.   Yang, Y. X.; Ochoa-Hernández, C.; O'Shea, V. A. D.; Pizarro, P.; Coronado, J. M.; Serrano, D. P., Effect of metal-support interaction on the selective hydrodeoxygenation of anisole to aromatics over Ni-based catalysts. *Appl. Catal. B: Environ.* **2014,** *145*, 91-100.

24.   Khromova, S. A.; Smirnov, A. A.; Bulavchenko, O. A.; Saraev, A. A.; Kaichev, V. V.; Reshetnikov, S. I.; Yakovlev, V. A., Anisole hydrodeoxygenation over Ni-Cu bimetallic catalysts: The effect of Ni/Cu ratio on selectivity. *Appl. Catal. A* **2014,** *470*, 261-270.

25.   Sankaranarayanan, T. M.; Berenguer, A.; Ochoa-Hernandez, C.; Moreno, I.; Jana, P.; Coronado, J. M.; Serrano, D. P.; Pizarro, P., Hydrodeoxygenation of anisole as bio-oil model compound over supported Ni and Co catalysts: Effect of metal and support properties. *Catal. Today* **2015,** *243*, 163-172.

26.   Ressler, T.; Wienold, J.; Jentoft, R. E.; Neisius, T., Bulk structural investigation of the reduction of MoO3 with propene and the oxidation of MoO2 with oxygen. *J. Catal.* **2002,** *210* (1), 67-83.

27.   Kyriakou, G.; Boucher, M. B.; Jewell, A. D.; Lewis, E. A.; Lawton, T. J.; Baber, A. E.; Tierney, H. L.; Flytzani-Stephanopoulos, M.; Sykes, E. C. H., Isolated Metal Atom Geometries as a Strategy for Selective Heterogeneous Hydrogenations. *Science* **2012,** *335* (6073), 1209-1212.

28.   Karim, W.; Spreafico, C.; Kleibert, A.; Gobrecht, J.; VandeVondele, J.; Ekinci, Y.; van Bokhoven, J. A., Catalyst support effects on hydrogen spillover. *Nature* **2017,** *541* (7635), 68-71.

29.   van der Hoeven, J. E.; Ngan, H. T.; Taylor, A.; Eagan, N. M.; Aizenberg, J.; Sautet, P.; Madix, R. J.; Friend, C. M., Entropic control of HD exchange rates over dilute Pd-in-Au alloy nanoparticle catalysts. *ACS Catal.* **2021,** *11* (12), 6971-6981.

30.   Marcella, N.; Lim, J. S.; Płonka, A. M.; Yan, G.; Owen, C. J.; van der Hoeven, J. E.; Foucher, A. C.; Ngan, H. T.; Torrisi, S. B.; Marinkovic, N. S., Decoding reactive structures in dilute alloy catalysts. *Nat. Commun.* **2022,** *13* (1), 1-9.

31.   Gao, J.; Zheng, Y. T.; Jehng, J. M.; Tang, Y. D.; Wachs, I. E.; Podkolzin, S. G., Identification of molybdenum oxide nanostructures on zeolites for natural gas conversion. *Science* **2015,** *348* (6235), 686-690.

32.   Yandulov, D. V.; Schrock, R. R., Catalytic reduction of dinitrogen to ammonia at a single molybdenum center. *Science* **2003,** *301* (5629), 76-78.

33.   Hu, H.; Wachs, I. E.; Bare, S. R., Surface structures of supported molybdenum oxide catalysts: characterization by Raman and Mo L3-edge XANES. *J. Phys. Chem.* **1995,** *99* (27), 10897-10910.

34.   Mouat, A. R.; Lohr, T. L.; Wegener, E. C.; Miller, J. T.; Delferro, M.; Stair, P. C.; Marks, T. J., Reactivity of a Carbon-Supported Single-Site Molybdenum Dioxo Catalyst for Biodiesel Synthesis. *ACS Catal.* **2016,** *6* (10), 6762-6769.

35.   Zhang, S.; Shan, J.-j.; Zhu, Y.; Frenkel, A. I.; Patlolla, A.; Huang, W.; Yoon, S. J.; Wang, L.; Yoshida, H.; Takeda, S., WGS Catalysis and In Situ Studies of CoO1‑x, PtCo n/Co3O4, and Pt m Co m′ /CoO1‑x Nanorod Catalysts. *J. Am. Chem. Soc.* **2013,** *135* (22), 8283-8293.

36.   Nguyen, L.; Zhang, S.; Wang, L.; Li, Y.; Yoshida, H.; Patlolla, A.; Takeda, S.; Frenkel, A. I.; Tao, F., Reduction of Nitric Oxide with Hydrogen on Catalysts of Singly Dispersed Bimetallic Sites Pt1Com and Pd1Con. *ACS Catal.* **2016,** *6* (2), 840-850.

37.   Tao, F. F.; Shan, J.-j.; Nguyen, L.; Wang, Z.; Zhang, S.; Zhang, L.; Wu, Z.; Huang, W.; Zeng, S.; Hu, P., Understanding complete oxidation of methane on spinel oxides at a molecular level. *Nat. Commun.* **2015,** *6* (1), 1-10.

38.   Wang, L.; Zhang, S.; Zhu, Y.; Patlolla, A.; Shan, J.; Yoshida, H.; Takeda, S.; Frenkel, A. I.; Tao, F., Catalysis and in situ studies of Rh1/Co3O4 nanorods in reduction of NO with H2. *ACS Catal.* **2013,** *3* (5), 1011-1019.

39.   Zhang, S.; Nguyen, L.; Liang, J.-X.; Shan, J.; Liu, J.; Frenkel, A. I.; Patlolla, A.; Huang, W.; Li, J.; Tao, F., Catalysis on singly dispersed bimetallic sites. *Nat. Commun.* **2015,** *6*, 7938.

40.   Patterson, A. L., The Scherrer Formula for X-Ray Particle Size Determination. *Phys. Rev.* **1939,** *56* (10), 978-982.

41.   Nguyen, L.; Tao, F., Reactor for tracking catalyst nanoparticles in liquid at high temperature under a high-pressure gas phase with X-ray absorption spectroscopy. *Rev. Sci. Instrum.* **2018,** *89* (2), 024102.

42.   Tang, Y.; Nguyen, L.; Li, Y.; Tao, F., In situ and operando study of catalysts during high-temperature high-pressure catalysis in a fixed-bed plug flow reactor with x-ray absorption spectroscopy. *Rev. Sci. Instrum.* **2023,** *94* (5).

43.   Tao, F.; Nguyen, L.; Tang, Y., Report on Photoelectron-Induced Excitation Spectroscopy and Its Close Correlation with Fundamental Studies of Catalysis. *J. Phys. Chem. C* **2022,** *126* (31), 13069-13087.

44.   Tao, F., *Application of Ambient Pressure X-ray Photoelectron Spectroscopy to Catalysis*. John Wiley & Sons: 2023.

45.   Weckhuysen, B. M., Determining the active site in a catalytic process: Operando spectroscopy is more than a buzzword. *Phys. Chem. Chem. Phys.* **2003,** *5* (20), 4351-4360.

46.   Jin, L.; Zheng, X.; Liu, W.; Cao, L.; Cao, Y.; Yao, T.; Wei, S., Integration of plasmonic and amorphous effects in MoO3−x spheres for efficient photoelectrochemical water oxidation. *J. Mater. Chem. A* **2017,** *5* (24), 12022-12026.

47.   Degler, D.; Pereira de Carvalho, H. W.; Weimar, U.; Barsan, N.; Pham, D.; Mädler, L.; Grunwaldt, J.-D., Structure–function relationships of conventionally and flame made Pd-doped sensors studied by X-ray absorption spectroscopy and DC-resistance. *Sens. Actuators, B* **2015,** *219*, 315-323.

48.   Chastain, J.; King, R. C.; Moulder, J. F., *Handbook of X-ray photoelectron spectroscopy: a reference book of standard spectra for identification and interpretation of XPS data*. Physical Electronics Division, Perkin-Elmer Corporation Eden Prairie, Minnesota: 1992.

49.   Toyoshima, R.; Yoshida, M.; Monya, Y.; Kousa, Y.; Suzuki, K.; Abe, H.; Mun, B. S.; Mase, K.; Amemiya, K.; Kondoh, H., In situ ambient pressure XPS study of CO oxidation reaction on Pd(111) surfaces. *J. Phys. Chem. C* **2012,** *116* (35), 18691-18697.

50.   Carlsson, A. F.; Naschitzki, M.; Bäumer, M.; Freund, H. J., The Structure and Reactivity of Al2O3-Supported Cobalt−Palladium Particles: A CO-TPD, STM, and XPS Study. *J. Phys. Chem. B* **2003,** *107* (3), 778-785.

51.   Marin-Flores, O.; Scudiero, L.; Ha, S., X-ray diffraction and photoelectron spectroscopy studies of MoO2 as catalyst for the partial oxidation of isooctane. *Surf. Sci.* **2009,** *603* (15), 2327-2332.

52.   Baltrusaitis, J.; Mendoza-Sanchez, B.; Fernandez, V.; Veenstra, R.; Dukstiene, N.; Roberts, A.; Fairley, N., Generalized molybdenum oxide surface chemical state XPS determination via informed amorphous sample model. *Appl. Surf. Sci.* **2015,** *326*, 151-161.

53.   Choi, J.-G.; Thompson, L. T., XPS study of as-prepared and reduced molybdenum oxides. *Appl. Surf. Sci.* **1996,** *93* (2), 143-149.

54.   Yan, G.; Sautet, P., Surface Structure of Co3O4 (111) under Reactive Gas-Phase Environments. *ACS Catal.* **2019,** *9* (7), 6380-6392.

55.   Chempath, S.; Bell, A. T., A DFT study of the mechanism and kinetics of methane oxidation to formaldehyde occurring on silica-supported molybdena. *J. Catal.* **2007,** *247* (1), 119-126.

56.   Prasomsri, T.; Nimmanwudipong, T.; Román-Leshkov, Y., Effective hydrodeoxygenation of biomass-derived oxygenates into unsaturated hydrocarbons by MoO3 using low H2 pressures. *Energy Environ. Sci.* **2013,** *6* (6), 1732-1738.

57.   Mironenko, A. V.; Vlachos, D. G., Conjugation-Driven "Reverse Mars-van Krevelen"-Type Radical Mechanism for Low-Temperature C-O Bond Activation. *J. Am. Chem. Soc.* **2016,** *138* (26), 8104-8113.

58.   Fu, J.; Lym, J.; Zheng, W.; Alexopoulos, K.; Mironenko, A. V.; Li, N.; Boscoboinik, J. A.; Su, D.; Weber, R. T.; Vlachos, D. G., C-O bond activation using ultralow loading of noble metal catalysts on moderately reducible oxides. *Nat. Catal.* **2020,** *3* (5), 446-453.

59.   Cohen, M.; Vlachos, D. G., Modified Energy Span Analysis Reveals Heterogeneous Catalytic Kinetics. *Ind. Eng. Chem. Res.* **2022,** *61* (15), 5117-5128.

60.   Merte, L. R.; Peng, G.; Bechstein, R.; Rieboldt, F.; Farberow, C. A.; Grabow, L. C.; Kudernatsch, W.; Wendt, S.; Lægsgaard, E.; Mavrikakis, M., Water-mediated proton hopping on an iron oxide surface. *Science* **2012,** *336* (6083), 889-893.

61.   Joubert, J.; Delbecq, F.; Thieuleux, C.; Taoufik, M.; Blanc, F.; Coperet, C.; Thivolle-Cazat, J.; Basset, J.-M.; Sautet, P., Synthesis, Characterization, and Catalytic Properties of γ-Al2O3-Supported Zirconium Hydrides through a Combined Use of Surface Organometallic Chemistry and Periodic Calculations. *Organometallics* **2007,** *26*, 3329-3335.

62.   Kozuch, S.; Shaik, S., How to conceptualize catalytic cycles? The energetic span model. *Acc. Chem. Res.* **2011,** *44* (2), 101-110.

63.   Kozuch, S.; Shaik, S., A combined kinetic−quantum mechanical model for assessment of catalytic cycles: Application to cross-coupling and Heck reactions. *J. Am. Chem. Soc.* **2006,** *128* (10), 3355-3365.

64.   Christiansen, J. A., The elucidation of reaction mechanisms by the method of intermediates in quasi-stationary concentrations. *Adv. Catal.* **1953,** *5*, 311-353.

65.   Mao, Z.; Campbell, C. T., Apparent activation energies in complex reaction mechanisms: a simple relationship via degrees of rate control. *ACS Catal.* **2019,** *9* (10), 9465-9473.

66.   Motagamwala, A. H.; Dumesic, J. A., Microkinetic modeling: a tool for rational catalyst design. *Chem. Rev.* **2020,** *121* (2), 1049-1076.

67.   Campbell, C. T., The Degree of Rate Control: A Powerful Tool for Catalysis Research. *ACS Catal.* **2017,** *7* (4), 2770-2779.

68.   Towns, J.; Cockerill, T.; Dahan, M.; Foster, I.; Gaither, K.; Grimshaw, A.; Hazlewood, V.; Lathrop, S.; Lifka, D.; Peterson, G. D.; Roskies, R.; Scott, J. R.; Wilkens-Diehr, N., XSEDE: Accelerating Scientific Discovery. Computing in Science & Engineering. *Comput. Sci. Eng.* **2014,** *16* (5), 62-74.

69.   Nystrom, N. A.; Levine, M. J.; Roskies, R. Z.; Scott, J. R. In *Bridges: a uniquely flexible HPC resource for new communities and data analytics*, Proceedings of the 2015 XSEDE Conference: Scientific Advancements Enabled by Enhanced Cyberinfrastructure, 2015; pp 1-8.

Catalytic Conversion of Biomass Derivatives

Anisole

Hydrogen

Hydrogen Activation

Anisole Activation

H spillover

Pd_1

Mo$_1$

TOC graphics

Higher Selectivity for Benzene

$Pd_1+Mo_1 > Pd_1 > Mo_1$